OPEN ACCESS



Comparison of the Core-collapse Evolution of Two Nearly Equal-mass Progenitors

Stephen W. Bruenn D., Andre Sieverding D., Eric J. Lentz D., Tuguldur Sukhbold D., W. Raphael Hix D., Leah N. Huk D., J. Austin Harris D., O. E. Bronson Messer D., and Anthony Mezzacappa D., and Anthony D., and Anthony D., and Anthony D., and Anthony Mezzacappa D., and Anthony D.

Abstract

We compare the core-collapse evolution of a pair of 15.8 M_{\odot} stars with significantly different internal structures, a consequence of the bimodal variability exhibited by massive stars during their late evolutionary stages. The 15.78 and 15.79 M_{\odot} progenitors have core masses (masses interior to an entropy of 4 $k_{\rm B}$ baryon⁻¹) of 1.47 and 1.78 M_{\odot} and compactness parameters $\xi_{1.75}$ of 0.302 and 0.604, respectively. The core-collapse simulations are carried out in 2D to nearly 3 s postbounce and show substantial differences in the times of shock revival and explosion energies. The 15.78 M_{\odot} model begins exploding promptly at 120 ms postbounce when a strong density decrement at the Si–Si/O shell interface, not present in the 15.79 M_{\odot} progenitor, encounters the stalled shock. The 15.79 M_{\odot} model takes 100 ms longer to explode but ultimately produces a more powerful explosion. Both the larger mass accretion rate and the more massive core of the 15.79 M_{\odot} model during the first 0.8 s postbounce time result in larger $\nu_e/\bar{\nu}_e$ luminosities and RMS energies along with a flatter and higher-density heating region. The more-energetic explosion of the 15.79 M_{\odot} model resulted in the ejection of twice as much ⁵⁶Ni. Most of the ejecta in both models are moderately proton rich, though counterintuitively the highest electron fraction ($Y_e = 0.61$) ejecta in either model are in the less-energetic 15.78 M_{\odot} model, while the lowest electron fraction ($Y_e = 0.45$) ejecta in either model are in the 15.79 M_{\odot} model.

Unified Astronomy Thesaurus concepts: Core-collapse supernovae (304); Explosive nucleosynthesis (503); Hydrodynamical simulations (767)

1. Introduction

The utility of models of supernovae (SNe) and other stellar phenomena are the insights they provide into parts of the star obscured from our view either by the star's outer precincts or the mists of time. Verification that such models can be trusted comes from the comparison to observations of the SNe or other events. For core-collapse supernovae (CCSNe), observations have long provided a set of gross properties of the SN, including the (kinetic) energy of the explosion, the total mass of the ejecta, the mass of ⁵⁶Ni in the ejecta, etc. (see, e.g., Hamuy 2003), although with uncertainties of several 10%. These large uncertainties make the data more useful for revealing general trends, like the correlation between increasing ejecta (and presumably stellar) mass, ⁵⁶Ni mass, and the explosion energy, than for providing detailed constraints of SN models. In recent years, the archive of galactic imagery from the Hubble Space Telescope has opened another opportunity for determining the mass of the star that subsequently exploded. Such information is critical to answer fundamental questions like which stars are responsible for SNe of various types and what are the initial mass functions of neutron stars (NSs) and black holes. The mass determination comes from a comparison between observational placement on the H-R diagram and evolutionary tracks from stellar evolution models (see Smartt 2009). The much smaller uncertainties from these

Original content from this work may be used under the terms of the Creative Commons Attribution 4.0 licence. Any further distribution of this work must maintain attribution to the author(s) and the title of the work, journal citation and DOI.

analyses allow useful comparisons between models and observations (see, e.g., Bruenn et al. 2016), however there are systematic uncertainties which need to be better understood, for example, the use of a different stellar evolution code shifts the stellar masses by $1-3~M_{\odot}(\text{Smartt 2015})$.

Addressing the same fundamental questions has also prompted several numerical studies of the progenitor dependence on the evolution of CCSNe with various numerical details and comprising various numbers of progenitors (O'Connor & Ott 2011; Ugliano et al. 2012; O'Connor & Ott 2013; Bruenn et al. 2016; Summa et al. 2016; Ott et al. 2018; Burrows et al. 2019, 2020; Vartanyan et al. 2021; Boccioli et al. 2022; Wang et al. 2022). Most crudely, the question is, for a given progenitor mass and structure, does an explosion occur or does collapse to a black hole prevent the explosion from becoming sufficiently powered? A more refined mapping might indicate, on average, the explosion energy, nucleosynthesis yields, and neutrino and gravitational wave signatures as functions of progenitor mass. What has become clear from the computational investigations thus far is that the CC evolution, even at the most basic level of whether or not an explosion ensues, is a nonmonotonic function of the progenitor mass because it is highly dependent on the core structure at the time of collapse. One challenge to these analysis is the unfortunate lack, at the present time, of convergence in the outcomes of different numerical simulations for a given progenitor. For example, note the differences in the CCSNe simulation outcomes initiated from four 12 to 25 M_{\odot} Woosley & Heger (2007) progenitors by Bruenn et al. (2016), Dolence et al. (2015), and Summa et al. (2016). It should be noted, however, that even large differences

(e.g., explosions versus duds) in the outcomes of CCSN simulations may indicate an extreme sensitivity of the outcomes to the details of the simulations, particularly if the models are close to the explosion criteria, rather than large differences between the simulation codes themselves.

Sukhbold et al. (2018) have further complicated the potential mapping between stellar mass and SN outcome by showing that shell-burning behaviors within the carbon core can generate stochastic variations in the final structure of the core for solar metallicity progenitors of 14–19 M_{\odot} . The goal of this paper is to compare the CC and subsequent evolution stemming from two progenitors of almost equal masses (difference in mass <0.1%) but different internal structures. A similar but very brief investigation of the consequences of internal structure differences for SN explosions was presented by Suwa et al. (2016), who evolved five 15 M_{\odot} progenitors provided by different stellar evolution groups. Because these differences in the Sukhbold et al. (2018) progenitors develop very late in the stars' lives, these models would be visually indistinguishable (their surface radii vary by less than 0.2%; surface temperature and density by less than 0.05%). This isolates the effects of the internal structure from those of stellar mass on the CC outcomes, providing a direct indicator of the sensitivity of the CC and subsequent evolution to the structure of a given mass progenitor. The variation of explosion outcomes for visually indistinguishable stars is also a measure of the physical scatter in these quantities we should expect for explosions coming from seemingly identical stars.

In Section 2 we examine the preSN evolution of two (15.78 and 15.79 M_{\odot}) updated Sukhbold et al. (2018) progenitors. Section 3 lays out the computational set up of our SN simulations from these progenitors. The basic properties of the CC and shock revival are presented in Section 4 and the dynamics of the explosions are presented in Section 5. A comparison of the basic nucleosynthesis of the two models is presented in Section 6, and a summary of the results of this paper is given is Section 7.

2. preSN Evolution

Inside the carbon core of massive stars there are episodes of core carbon, neon, oxygen, and silicon burning, each followed by shell-burning episodes. These burning regions can influence concurrent and ensuing episodes, making for stochasticity in the evolution of massive star cores. Sukhbold et al. (2018) identified some of the variability as being bimodal and related to specific patterns of shell interactions. A useful quantity to characterize the core of a massive star is the mass of the region where the entropy $s < 4 k_{\rm B} {\rm baryon}^{-1}$, which as often been used to estimate the remnant mass, or mass cut, for parameterized explosions in spherical symmetry (Woosley & Heger 2007) and for a criterion to estimate the likelihood of a successful, neutrino-driven explosion (Ertl et al. 2016). The multivalued, branched nature of M_4 for helium core masses, $M_{\rm He}$, in the range of 4.4–4.6 M_{\odot} can be clearly seen in Figure 1. In both branches, M_4 , which is typically tied to the mass coordinate of maximum oxygen burning at collapse, increases with $M_{\rm He}$, while a clear gap remains. This is true both of the small network models from Sukhbold et al. (2018) (gray) and the unpublished models using a larger network, shown in green. The unpublished "large network" models incorporate an adaptive nuclear network of up to 300 species as needed into the evolution of the stellar structure equations instead of the 19

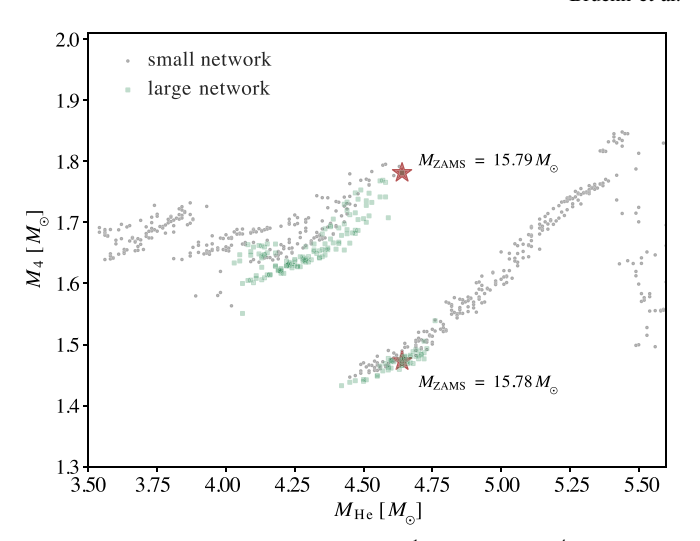
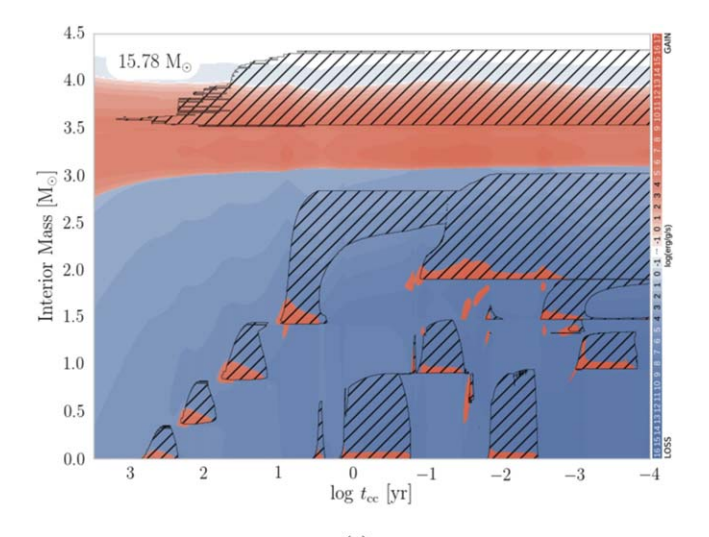


Figure 1. Mass with entropy $s < 4 k_{\rm B}$ baryon⁻¹(M_4) plotted vs. ⁴He core mass ($M_{\rm He}$) for the small network models of Sukhbold et al. (2018) (gray circles) and the large network models of T. Suhkbold (unpublished; green squares). The two models used in this paper are marked with stars.

species network supplemented by the quasi-equilibrium network for silicon burning for the "small network" runs as detailed in Section 2.2 of Sukhbold et al. (2018), but are otherwise identical in numerical configuration. The two models from which we will compute the SNe are on different branches despite differing in initial mass by only 0.01 M_{\odot} . The upper branch at $M_{\rm He} = 4.5~M_{\odot}$ contains the 15.79 M_{\odot} model near its upper mass limit with $M_4 = 1.78~M_{\odot}$ and the lower branch contains the 15.78 M_{\odot} model with $M_4 = 1.47~M_{\odot}$.

Figure 2 shows the convective histories (Kippenhahn diagrams) of the two models, where the hatched areas indicate convective regions, the red color indicates heating by nuclear burning, and the blue color cooling by neutrino emission. About 1000 yr before collapse, both models ignite convective core C burning followed by three C-burning shells moving outward in mass. While the third C-burning shell is active, Ne burning takes place in the core and the end of the shell-burning episode is coincident with the start of core oxygen burning at about one year before collapse. Both models, and the two M_4 branches to which they belong, are characterized by the suppression of core oxygen burning until the third carbonburning shell is complete due to the ignition of that shell within the degenerate effective Chandrasekhar mass. This is unlike the branch for $M_{\rm He} < 3.7~M_{\odot}$ (see Figure 1), where the C-burning shell ignition occurs outside the Chandrasekhar mass and does not suppress core oxygen burning. After core O burning, the evolutions of the two models we consider here diverge. In the 15.78 M_{\odot} model, a fourth convective C-burning shell ignites about 0.1 yr before collapse, encompassing the region between $2 M_{\odot}$ and $3 M_{\odot}$ at the same time as the first O shell ignites. This leads to a flat ¹²C profile in this region (see Figure 3). This C-shell-burning episode slows the contraction of the core and suppresses the second O-burning shell and leads to an initial Si core that is smaller than in the 15.79 M_{\odot} model, in which the fourth C-burning shell only ignites about 8 hr before collapse and leaves behind gradients in the ¹²C mass fraction profile. In both models, the final O-shell-burning episode before collapse then takes place on top of this Si core. The difference in the Sicore sizes at the time of Si-core burning is also highlighted in Figure 13 of Sukhbold et al. (2018) and it is closely connected to the entropy jump that defines the value of M_4 . The



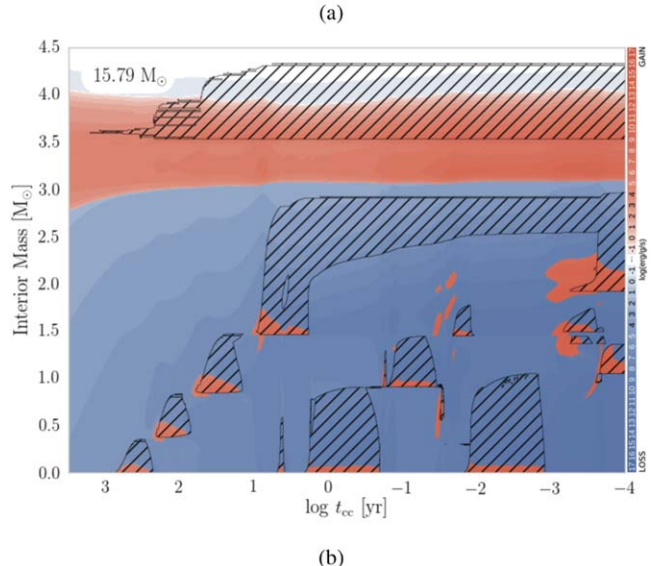


Figure 2. Carbon-core convective histories of the (a) 15.78 M_{\odot} and (b) 15.79 M_{\odot} preSN models.

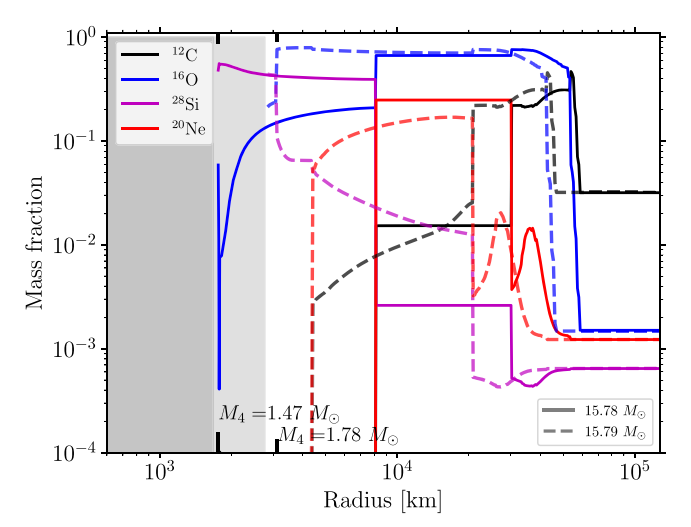


Figure 3. Mass fraction profiles of the two progenitors. The thick tickmarks at 1.47 M_{\odot} and 1.78 M_{\odot} indicate M_4 for the 15.78 M_{\odot} and the 15.79 M_{\odot} models, respectively. The composition of the Fe core in NSE is not shown.

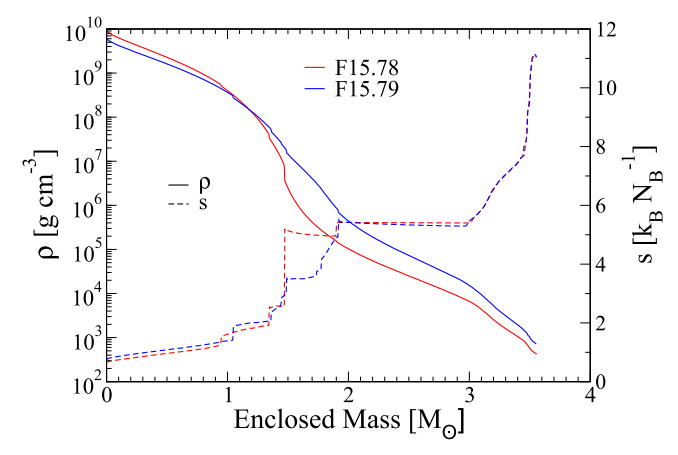


Figure 4. The density and entropy profiles of the progenitors.

suppressed second oxygen-burning shell thus gives rise to the lower branch in Figure 1 where the 15.78 M_{\odot} model is located. At the time of collapse, in the 15.78 M_{\odot} model, oxygen is not completely exhausted in the region already dominated by Si, and as consequence M_4 is located at 1.47 M_{\odot} , inside the final Si core (see Figure 3), which is very extended, reaching out to 8000 km. In the 15.79 M_{\odot} model, on the other hand, M_4 is at $1.78 M_{\odot}$, about 3000 km from the center and still aligned with the edge of the Si core at the time of collapse. Not surprisingly, having more mass concentrated in a smaller volume has a significant effect on the density. As Figure 4, illustrates, above fairly similar iron cores, the density structures of the 15.78 and 15.79 models are quite different in the silicon- and oxygen-rich regions. Most notable is a sharp drop in density of the 15.78 M_{\odot} model at an enclosed mass of 1.47 M_{\odot} , where the base of the powerful convective oxygen-burning episode was located just prior to collapse. The most significant difference in the entropy profiles of these models (Figure 4) corresponds to this density drop, making clear the cause of the difference in M_4 .

Of particular importance for the postcollapse evolution of these models is the difference in their compactness, defined as $\xi_M = (M/M_{\odot})/(R(M)/1000 \text{ km})$. Smaller compactness has been suggested as an indicator of easier explodability by O'Connor & Ott (2011), at least for progenitors of the same or very similar zero-age main-sequence masses (Vartanyan et al. 2021). For the 15.78 and 15.79 M_{\odot} models, $\xi_{2.5} = 0.136$ and 0.206, respectively, and 0.301 and 0.604 for $\xi_{1.75}$. The parameterized simulations of O'Connor & Ott (2011) indicated that a progenitor having a compactness parameter $\xi_{2.5} > 0.45$ would lead to black hole formation rather than an explosion. Other more elaborate criteria for the explodability of a given progenitor have been developed by (e.g., Ertl et al. 2016; Muller et al. 2016; Suwa et al. 2016; Boccioli et al. 2022; Wang et al. 2022), and they led to similar conclusions regarding the explodability of the 15.78 M_{\odot} model versus that of the 15.79 M_{\odot} model.

3. Neutrino-radiation Hydrodynamics

The SN simulations that follow were computed using the CHIMERA neutrino-radiation hydrodynamics code (Bruenn et al. 2020) and are part of the CHIMERA "F-series" of simulations. CHIMERA uses PPMLR hydrodynamics, multipole

self gravitation with a monopole GR potential correction, rayby-ray four-species neutrino transport by the flux-limited diffusion method, a dense nuclear equation of state (EoS) at high temperatures where nuclear statistical equilibrium (NSE) applies and a nuclear network where it does not.

The neutrino opacities used are those used since the B-series simulations (Bruenn et al. 2013, 2016) with an improvement to the nucleon–nucleon bremsstrahlung computation. For bremsstrahlung, we have modified the formulation in Hannestad & Raffelt (1998) to treat nn-, pp-, and np-bremsstrahlung separately with the appropriate degeneracy factors.

The NSE EoS is the SFHo EoS of Steiner et al. (2013) incorporated into CHIMERA (Landfield 2018) using the WeakLib⁶ framework via the CompOSE⁷ database. As in the Series-E runs (Landfield 2018; R. E. Landfield et al. 2023, in preparation), we use the Cooperstein (1985) electron EoS with SFHo and also in the nonNSE network region for continuity.

The nuclear network is the anp56 network used in the D-series and E-series (R. E. Landfield et al. 2023, in preparation) simulations. It contains the same $14~\alpha$ -chain nuclei ($^4\mathrm{He},\ ^{12}\mathrm{C}-^{60}\mathrm{Zn}$) as the alpha network used in the B-series (Bruenn et al. 2013, 2016) and C-series (Lentz et al. 2015) with the neutron, proton, and $^{56}\mathrm{Fe}$ added actively, but nonreactively, to the network. The inclusion of these three "inert" species, which are not connected by reactions to the rest of the network, allows us to compute NSE compositions directly with the XNet nuclear network when needed at the boundary of the NSE region, rather than extracting them from the NSE EoS.

Together with internal code updates, this constitutes the default physical inputs and code for Series-F CHIMERA simulations.

Initial conditions for the CC and SN calculations with CHIMERA are taken from the 15.78 and 15.79 M_{\odot} preSN progenitors described above. In the following, we will refer the SN simulations by their CHIMERA model designations F15.78 and F15.79. The inner 3.56 M_{\odot} of both progenitors out to the ⁴He shell, with radii of 61,250 km for F15.78 and 48,960 km for F15.79, were remapped onto 720 radial shells of unequal widths that generally increase with radius. The simulations were carried out in full 2D with 240 zones of uniform width (0.75) in θ from the onset of collapse. The small roundoff errors supply the perturbations from which the fluid instabilities grow. It is well known that imposing axisymmetry results in unipolar or bipolar deformations along the symmetry axis due to the boundary conditions imposed at the poles, which deflect fluid motions parallel to the pole. In addition, the inverse turbulent energy cascade distributes the energy in an unphysical way to the largest scales (see Kraichnan 1967; Hanke et al. 2012; Couch 2013; Couch & Ott 2015) Nevertheless, 2D simulations have manifested similarities in overall explosion outcomes (Muller 2015; Burrows et al. 2019; Vartanyan et al. 2019), are relatively fast now, and are useful for obtaining insights concerning the interplay of essential physics and, if interesting, can motivate future 3D simulations.

4. Onset of Explosion

The shock trajectories of both models, Figure 5(a), are quite similar from bounce through shock stagnation at a radius of \sim 160 km, reflecting the similar structure of their iron cores.

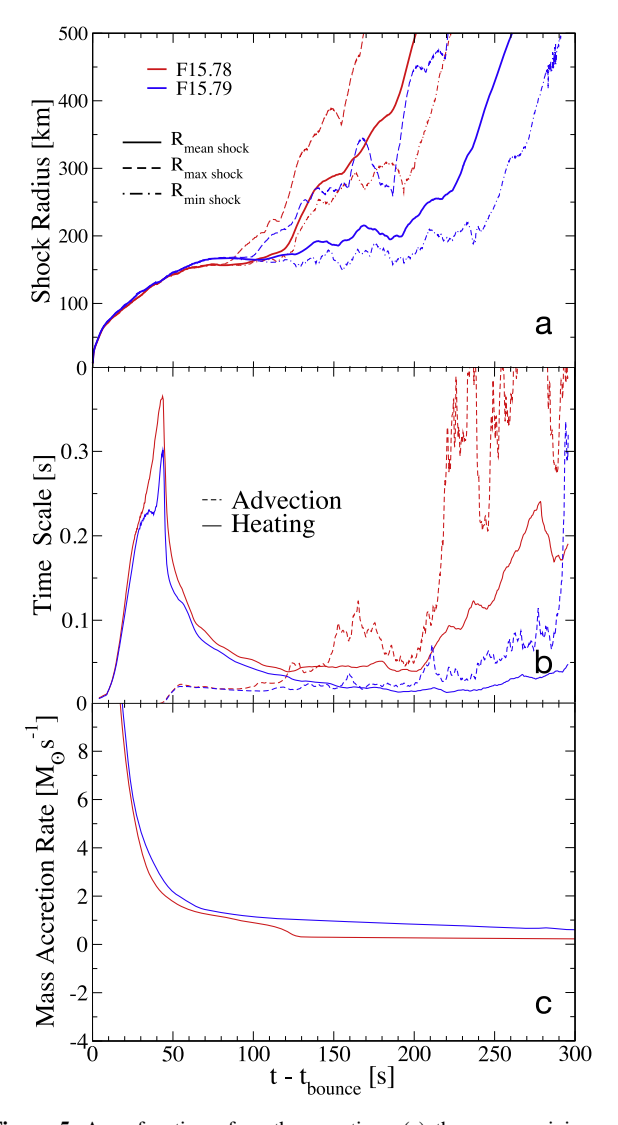


Figure 5. As a function of postbounce time, (a) the mean, minimum, and maximum shock positions as a function of postbounce time, (b) the advection and heating timescales, and (c) the mass accretion rate at the shock location. The red and blue lines correspond, respectively, to F15.78 and F15.79.

Following stagnation, the shock location is set by the quasisteady-state balance between the accretion ram pressure at the shock and the total pressure, thermodynamic and turbulent, of the immediate postshock material. In the neutrino-driven mechanism for CCSNe, the postshock pressure is generated by the deposition of energy into the heating region by neutrinos. The revival of the stationary (stalled) shock will occur when the total postshock pressure (thermal and turbulent) begins to exceed the preshock accretion ram pressure to the point where a stationary solution for the shock radius no longer exists (Burrows & Goshy 1993; Janka & Müller 1996; Janka 2001, 2012; Summa et al. 2016). The different epochs and modes of shock revival for the two models are a consequence of the different density structures of their progenitors, shown in Figure 4. For F15.78 (with the smaller compactness parameter), shock revival occurs at 120 ms (unless otherwise specified all times refer to postbounce times) when the density decrement at the Si-Si/O interface at 1.47 M_{\odot} is advected through the shock, resulting in a sudden drop in

https://code.ornl.gov/astro/weaklib-tables

https://compose.obspm.fr

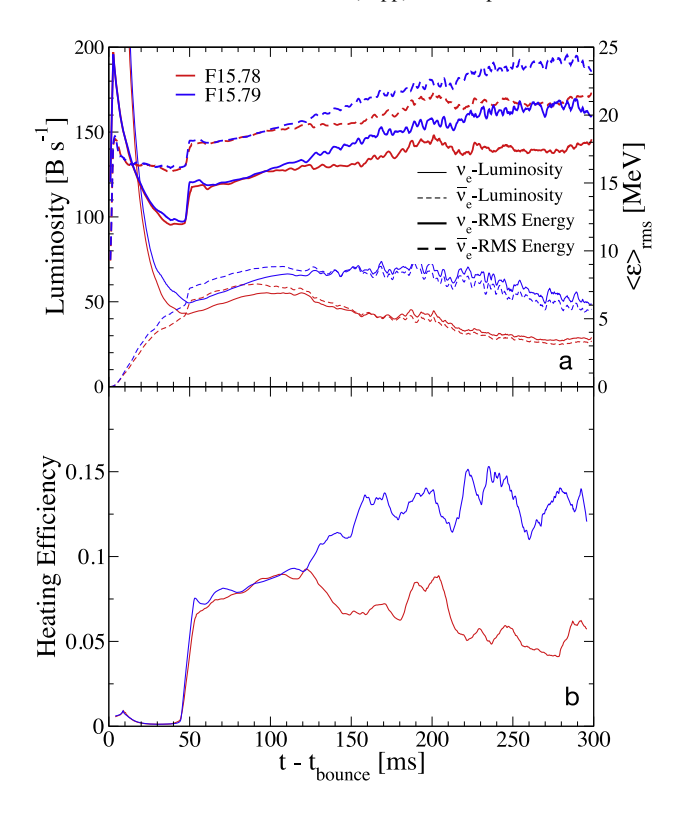


Figure 6. As a function of postbounce time, (a) the ν_e and $\bar{\nu}_e$ luminosities and RMS energies at the gain radius and (b) the neutrino heating efficiency.

the mass accretion rate at the shock front (Figure 5(c)). The sudden decline in the ram pressure ahead of the shock along with the still significant mass accretion luminosity from the surface of the protoNS is the trigger for shock revival in this model. Lacking a density decrement, there is no corresponding sudden decrease in the accretion ram to trigger shock revival in F15.79. In this model, shock revival occurs about 100 ms later than in F15.78, following a period during which the continuing core and accretion luminosities, coupled with a gradual hardening of the ν_e and $\bar{\nu}_e$ spectra (Figure 6(a)), continue to pump energy into the postshock region. Eventually an accretion/luminosity critical condition is satisfied (as formulated for 1D by Burrows & Goshy 1993; and extended to multiD by Muller & Janka 2015; Summa et al. 2016) and shock revival ensues.

This description of the onset of shock revival is reflected in the often used timescale inequality criterion. Shock revival is triggered when the advection or dwell timescale, τ_{adv} , of a fluid element in the gain region, the region inside the shock where heating exceeds cooling, becomes longer than the heating timescale, τ_{heat} , the timescale for an e-fold increase in the total energy of a fluid element by neutrino heating (Janka et al. 2001; Thompson et al. 2005; Buras et al. 2006; Fernández 2012). With $\tau_{\rm adv}$ approximated as $M_{\rm gain}/\dot{M}$, where steady-state conditions are assumed, and $au_{\rm heat} = E_{\rm gain}/\dot{Q}_{\rm gain},$ where $E_{\rm gain}$ and $\dot{Q}_{\rm gain}$ are the integrated total energy and the integrated net heating rate of material in the gain layer, respectively, these timescales are plotted for both models in Figure 5(b). The sudden switch from $\tau_{adv} < \tau_{heat}$ to $\tau_{adv} > \tau_{heat}$ at 120 ms for F15.78 is brought about by the abrupt increase in $\tau_{\rm adv}$ due to the advection of the density decrement through the shock and its immediate consequent expansion. Absent a density decrement trigger, no such sudden increase in $\tau_{\rm adv}$ is observed for F15.79 until 210 ms. Rather, there is a sustained period from 120 to 210 ms during which $\tau_{\rm adv}$ slowly increases and $\tau_{\rm heat}$ slowly decreases, indicating a heating-driven build up of internal energy and pressure inside a slowly expanding heating region. At 210 ms, $\tau_{\rm adv}$ exceeds $\tau_{\rm heat}$ sufficiently for shock revival to occur.

Another indicator of shock revival dynamics is the heating efficiency, η_b defined by

$$\eta_f = \frac{\dot{\mathcal{Q}}}{L_{\nu_e} + L_{\bar{\nu}_e}},\tag{1}$$

and plotted for the two models in Figure 6(b). As before, \dot{Q} is the net neutrino energy deposition rate in the gain region, the region inside the shock where the neutrino energy deposition exceeds emission, and L_{ν_e} and $L_{\bar{\nu}_e}$ are the ν_e and $\bar{\nu}_e$ luminosities at the base of the gain region, respectively. Until the density decrement of F15.78 reaches the shock at 120 ms, the heating efficiencies for both models are quite similar, reflecting their similar core structures at bounce and the similar rates of mass advection through the shock during this time. The heating efficiencies rise during this time primarily because of the increase in the neutrino RMS energies, as shown in Figure 6(a). The decline in η_f for F15.78 after 120 ms is due to a combination of the leveling off of its neutrino RMS energies (Figure 6(a)) and the decline in the density of the heating region following the expansion of the shock. The continuing rise in the ν_e and $\bar{\nu}_e$ RMS energies in F15.79 past 120 ms leads to increasing heating efficiency (Figure 6(b)) that persists until the occurrence of shock revival for this model at 210 ms, similar to earlier CHIMERA models (Bruenn et al. 2013; Lentz et al. 2015) where the shock also revived without a sudden drop in ram pressure.

Fluid instabilities have long been known to play a key role in enhancing the possibility of shock revival by increasing the dwell time of material in the gain region, thereby increasing the time and efficiency at which material can absorb energy. The addition of turbulent pressure via the radial Reynolds stress behind the shock, together with the thermal pressure, also facilitates pushing the shock outward (Burrows & Hayes 1996; Couch & Ott 2015; Nagakura et al. 2019). The neutrino-heated layer develops a negative entropy gradient which can render it convectively unstable (Herant et al. 1994; Burrows & Hayes 1996; Janka & Müller 1996) when the convective growth rate exceeds the rate at which accreting material is swept through the gain region, parameterized by Foglizzo et al. (2006)

$$\chi = \int_{\langle R_s \rangle}^{\langle R_s \rangle} \frac{\text{Im } \langle \omega_{\text{BV}} \rangle}{|\langle \nu_r \rangle|}.$$
 (2)

Foglizzo et al. (2006) showed that when $\chi \gtrsim 3$ convective growth is expected to overcome the stabilizing effect of matter inflow, which we see at 69 ms for F15.78 and 75 ms for F15.79. These times correlate well with the first appearance of stable convective structures in the gain region of our models. Convection persists for only about 50 ms before runaway shock expansion sets in for F15.78, driven by the density decrement, and about 150 ms for F15.79.

The standing accretion shock instability (SASI), first investigated in the context of shock revival in CCSNe by Blondin et al. (2003) and further investigated (Foglizzo et al. 2006; Ohnishi et al. 2006; Foglizzo et al. 2007; Yamasaki & Yamada 2007; Scheck et al. 2008, and many subsequent works), can also be important in promoting conditions for shock revival by establishing large-scale postshock flows that periodically push the shock outward (Blondin et al. 2003). The dipole and quadrupole modes of the shock surface appear in both models and the periods match the periods computed using the formulation for SASI periods in Ohnishi et al. (2006) and Scheck et al. (2008), compensating for neutrino heating as Yamasaki & Yamada (2007) suggest. This suggests that the SASI is present in both of our models, but as is typical in CCSN simulations with strong neutrino-driven convection, we cannot assess the relative importance of the SASI in aiding explosion.

Both of our models follow the typical early pattern for postbounce evolution—shock stagnation, development of neutrino-driven convection and SASI oscillations of the shock, a slow increase in the neutrino heating efficiency, and postshock thermal heating. At this point, differences in the ρ (M) versus M profiles of the two models, illustrated in Figure 4, cause the subsequent evolutionary scenarios of the two models to diverge. The large decrement in density at 1.47 M_{\odot} in the 15.78 M_{\odot} progenitor created by a late precollapse oxygenshell-burning episode terminates the slow prerevival build up to explosion in F15.78 when that layer accretes through the shock. A rapid drop in the external ram pressure results, followed by a sudden expansion of the shock, and triggering the explosion directly. The 15.79 M_{\odot} progenitor did not have such a lateburning episode, nor the resulting density decrement, so the explosion in F15.79 is only triggered through a slower process of pressure build up from neutrino heating and a more gradual decline in ram pressure at the shock until a critical condition is reached. This provides the first major impact of the structural differences in these two progenitors, resulting in the differences in the explosions generated.

Recent work has investigated the effect of progenitor asphericities due to precollapse convection in oxygen- and silicon-burning shells on the postcollapse evolution of CCSNe (Couch & Ott 2013, 2015; Muller & Janka 2015; Abdikamalov et al. 2016; Müller 2016; Muller et al. 2017; Vartanyan et al. 2018). While the exact mechanism still needs to be elaborated, this work indicates that vigorous large-scale convection in precollapse progenitors will shorten the time to shock revival for successful models and increase the possibility of shock revival for those models which would otherwise not explode. It is doubtful that incorporating convection in the oxygen- or silicon-burning shells in the F15.78 progenitor would have much effect on its shock-revival time, as a robust shock revival already ensues shortly after bounce when the density decrement at the Si/Si-O interface encounters the shock. For F15.79, shock revival occurs while the shock is still within the extensive Si shell, so vigorous convective burning in this shell might reduce the time for shock revival.

5. Explosion Dynamics

In this section we will give an overview of the evolutionary differences between the two models followed in subsequent sections by a detailed look at the origin of these differences,

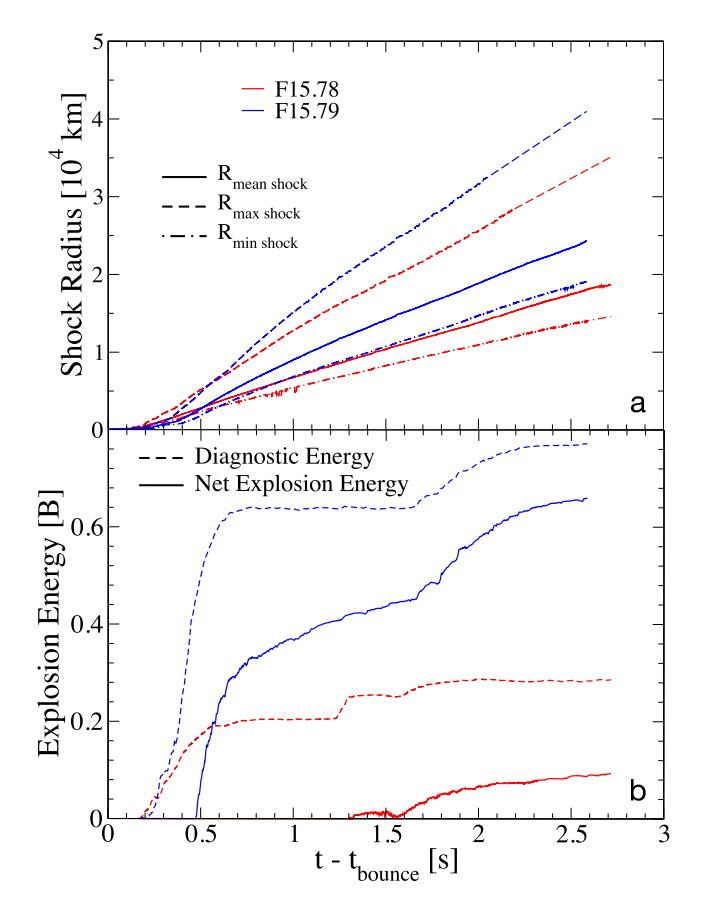


Figure 7. Comparison of the (a) mean, minimum, and maximum radii of the shocks of both models and (b) the diagnostic and net explosion energies, as a functions of postbounce time.

tracing them back to differences in the internal structures of their progenitors.

5.1. Overview

Following shock revival, the dynamic evolutions of the two models are considerably different, as exemplified by the difference in shock trajectories (Figure 7(a)) and in the explosion-energy histories (Figure 7(b)). The shock grows faster in F15.79 after the explosion in that model is finally launched, catching up with the (mean) shock radius of F15.78 about 0.5 s after bounce. The "diagnostic energy" is the sum of the total energies (gravitational, internal, and kinetic) of all zones for which this energy is positive (Buras et al. 2006; Müller et al. 2012; Bruenn et al. 2013). The net explosion energy is the diagnostic energy plus the (negative) binding energy of the on- and off-grid material ahead of the shock (Bruenn et al. 2013). (See Appendix A of Bruenn et al. 2016 for the full details of the energies used). While the growth rates of the diagnostic energy are similar up to 0.3 s after bounce, the growth rate in F15.79 then accelerates while the growth rate in F15.78 declines. Both measures of the explosion energy therefore become much larger in F15.79, with the diagnostic energy more than $3 \times$ larger at 1 s after bounce and $\approx 2.5 \times$ by the end of the simulations. By the end, an even greater difference (\approx 7×) develops in their net energies. In neither model has the net energy leveled off by the end of the simulations, but if they do not change significantly during further evolution (however, see Muller 2015) F15.79 is within

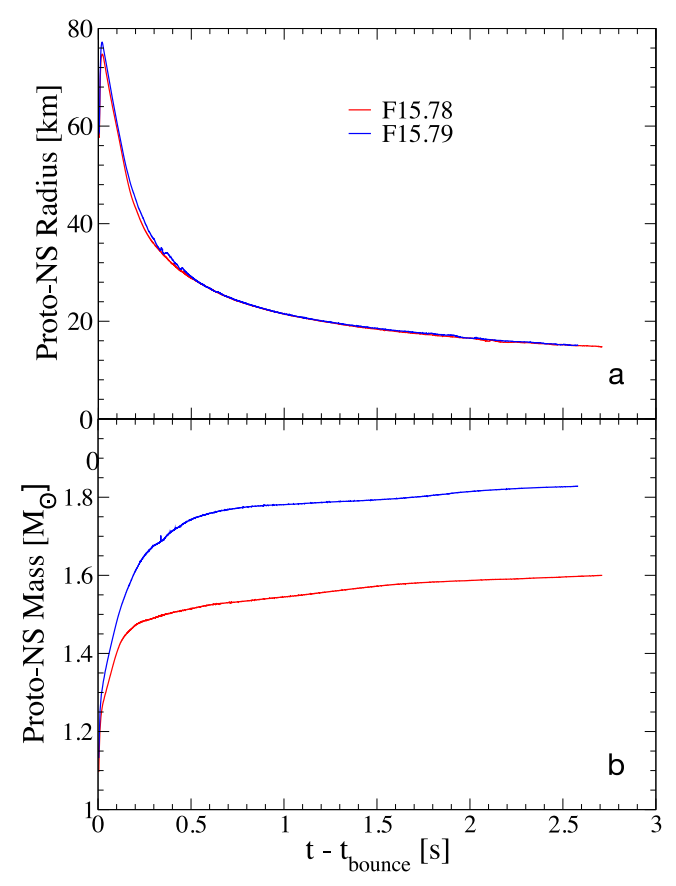


Figure 8. Comparison of the (a) protoNS radii, and (b) protoNS masses of the two models as a function of postbounce time.

the observed range of explosion energies for $M_{\rm MS}\sim 16~M_{\odot}$ (Martinez et al. 2022) while F15.78 falls below this observed range.

The protoNS radii (Figure 8(a)) of the two models are strikingly similar, while the baryonic masses (Figure 8(b)) are substantially different. (Following common practice, we use the region with density $>10^{11}$ g cm⁻³ to define the protoNS.) The baryonic masses are still slowly increasing at the end of the simulations, at this time having attained values of 1.59 and 1.82 M_{\odot} for F15.78 and F15.79, respectively, which correspond to cold-NS gravitational masses of 1.46 and 1.62 M_{\odot} using the approximation formula of Timmes et al. (1996). These masses are in the range of the observed distribution of slowly rotating pulsars (Schwab et al. 2010; Özel et al. 2012; Özel & Freire 2016). While less closely constrained than the masses of binary NSs, slowly rotating pulsars seem a more likely outcome for single, nonrotating progenitor stars.

The neutrino luminosities and RMS energies for the duration of the simulation are shown in Figure 9 for the two models. There are clearly substantial differences between these quantities for the two models in the period from 0.2 to 0.8 s and again from 1.6 to 2.3 s, with these quantities being larger for F15.79. These differences are important to the strength of the explosion, as they partially account for the heating rate and heating efficiency differences between the two models that will be explored in detail below.

Figure 10 displays the morphological evolution of the two models by means of 2D entropy plots. At 0.1 s, both models exhibit neutrino-driven convection, more highly developed in F15.78. By 0.3 s, both models have evolved into a highly

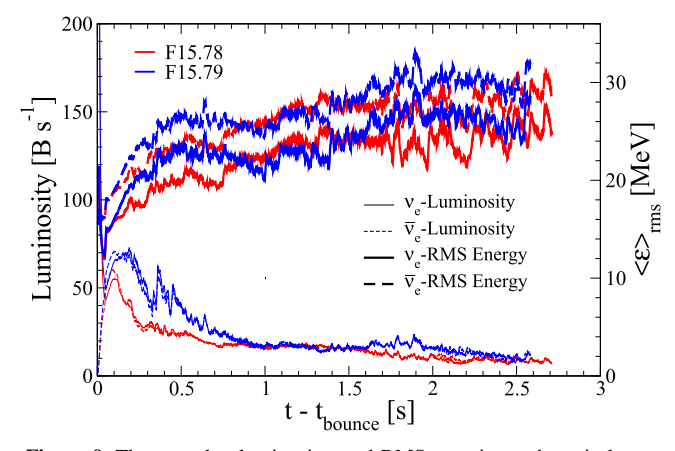


Figure 9. The ν_e and $\bar{\nu}_e$ luminosites and RMS energies at the gain layer.

prolate configuration with F15.78 having expanded farther at this time. At 1 s, both models have expanded much farther with F15.79 having overtaken F15.78. F15.78 has become almost unipolar at this time, the transition from bipolar to unipolar occurring roughly between 0.4 and 0.6 s, while F15.79 remains clearly bipolar.

Considering the diagnostic energies of the two models (Figure 7(b)) again, it is clear that the major differences between the two models get established during the first 0.6 s. Our primary focus in Sections 5.2–5.7 will therefore be to examine the origin of these evolutionary differences during this period, relating them to differences in the progenitors. In Section 5.8, we will take a look at the causes for the later jumps in the diagnostic energy at \approx 1.2 s and \approx 1.55 s in F15.78 and at \approx 1.65 s in F15.79.

5.2. Heating Rates

To understand how two nonrotating progenitors with almost equal masses have such dissimilar explosion energy histories during the first 0.6 s, we begin with the basic driver of the explosion, the neutrino heating rate \dot{Q}^+ . Neutrino heating can be expressed as an integral over the gain region of the volume-specific heating rate \dot{q}^+ , whose dominant contribution is given by

$$\dot{q}^{+} = \left\{ \frac{X_{\rm n}}{\lambda_0^a} \frac{L_{\nu_{\rm e}}}{4\pi r^2} \frac{\langle E_{\nu_{\rm e}}^2 \rangle}{\langle \mathcal{F}_{\nu_{\rm e}} \rangle} + \frac{X_{\rm p}}{\bar{\lambda}_0^a} \frac{L_{\bar{\nu}_{\rm e}}}{4\pi r^2} \frac{\langle E_{\bar{\nu}_{\rm e}}^2 \rangle}{\langle \mathcal{F}_{\bar{\nu}_{\rm e}} \rangle} \right\} \frac{\rho}{m_{\rm B}},\tag{3}$$

where $X_{\mathrm{n/p}}$ are the neutron and proton mass fractions, $L_{\nu_e/\bar{\nu}_e}$ and $E_{\nu_e/\bar{\nu}_e}$ are the ν_e and $\bar{\nu}_e$ luminosities and energies, respectively, $\langle E_{\nu_e/\bar{\nu}_e}^2 \rangle \equiv \langle E_{\nu_e/\bar{\nu}_e}^3 \rangle / \langle E_{\nu_e/\bar{\nu}_e} \rangle$, $\mathcal{F}_{\nu_e/\bar{\nu}_e}$ are the ν_e and $\bar{\nu}_e$ inverse flux factors (inverse ratios of the first to the zeroth angular moments of the neutrino distribution), m_{B} is the mean baryon mass, and λ_0^a , $\bar{\lambda}_0^a$ are weak interaction constants related to the absorption mean free path. The quantities in angle brackets are spectral energy averages.

The total net neutrino heating rates for the two models are shown in Figure 11(a). The rates for the two models are practically the same and essentially zero for the first 50 ms postbounce, after which they are within 15%-20% of each other until 120 ms postbounce. At this point, the hearing rates for both models undergo a ~ 0.5 s duration peak with the heating rates for F15.79 exceeding those of F15.78 by a factor of 2–3 until ≈ 0.6 s postbounce. These heating rate peaks are

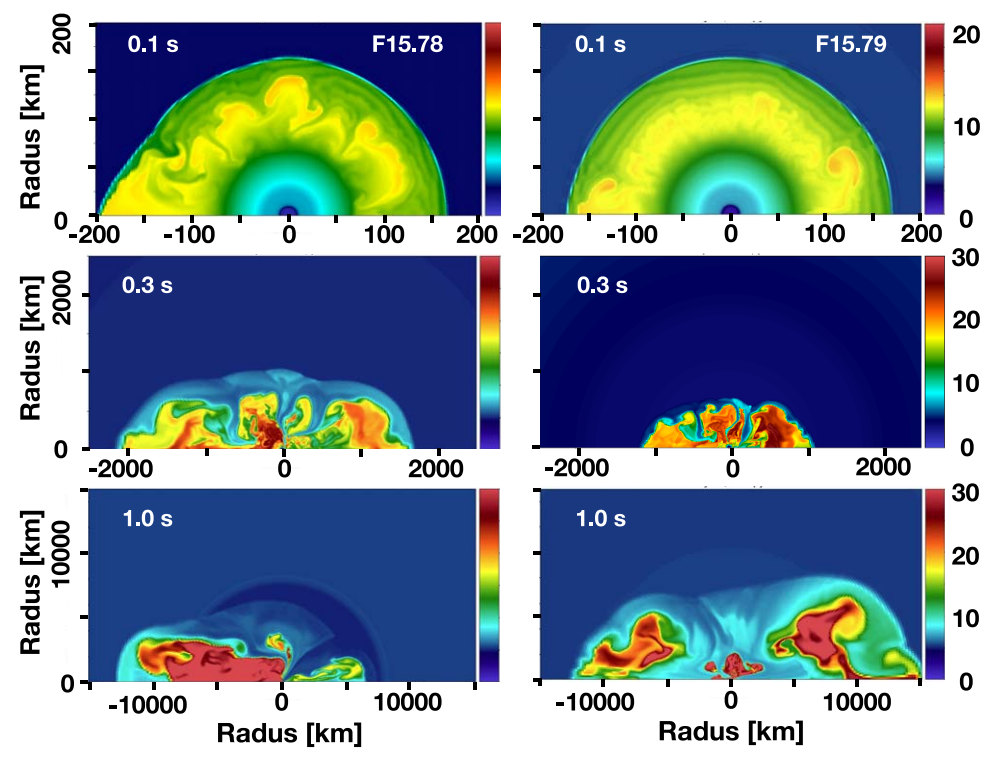


Figure 10. Specific entropy of F15.78 and F15.79 at postbounce times of 0.1, 0.3, and 1.0 s. The radial scales are the same for both models and are 0–200 km for the 0.1 s plot, 0–2500 km for the 0.3 s plot, and 0–15,000 km for the 1.0 s plot.

coincident with the major rises in the diagnostic energies of the models (Figure 7(b)). Both heating rates are relatively small beyond \approx 0.6 s postbounce except for a brief rise in the rate for F15.78 at \approx 1.2–1.3 s and a rise in the F15.79 rate from \approx 1.65–2.3 s, which will be discussed in Section 5.8.

To examine the origin of the differences in the heating rates between the two models, we compare each of the factors that determine these rates as given by Equation (3), namely, the radius r, the neutrino luminosities and RMS energies, the neutron and proton mass fractions, the flux factors, and the gain region masses.

The compositional mass fraction and neutrino flux factor differences do not contribute much to the differences in the heating rates. The matter throughout much of the gain region consists of free neutrons and protons, so the sum of the nucleon mass fractions, X_n and X_p in Equation (3) is unity. The partitioning of the nucleons between X_n and X_p depends on the the value of the electron fraction, Y_e at the gain radius (Figure 11(b)), which is about 10% larger for F15.79 from 0.5 to 0.9 s and otherwise nearly the same in both models. The factors multiplying X_n and X_p in Equation (3) differ by as much as 16%, due mainly to the luminosity and RMS energy differences (Figures 6(a) and 9), but when multiplied by a maximum 10% difference in the mass fractions, the net contribution to the heating rate differences is rather minor. The flux factors depend, to first order, on the ratio of the neutrinosphere radii to the gain layer radii, and these are approximately the same as a function of postbounce time for the two models.

The primary cause for the heating rate differences is the differences in the ν_e and $\bar{\nu}_e$ luminosities and RMS energies of the two models, shown in Figures 6(a) and 9. The neutrino quantities for F15.79 exceed those for F15.78 from \approx 0.2 s to \approx 0.8 s, and again from \approx 1.6 s to \approx 2.3 s, reflecting

approximately the same difference pattern in the neutrino heating rates shown in Figure 11(a). The ν_e and $\bar{\nu}_e$ luminosity and RMS energy differences collectively account for about a factor of 2 difference in the heating rates in the first 0.6 s.

The other primary contribution to the heating rate differences between the two models is the difference in their gain region masses (Figure 11(c)), defined here as the mass lying between the gain layer and the surface enclosing 90% of the heating rate (Figure 12). Like the ν_e and $\bar{\nu}_e$ luminosities and RMS energies, the mass of the gain region for F15.79 exceeds that of F15.78 by as much as a factor of 2 until about 0.9 s. This can be traced to the larger densities in the matter surrounding the inner core of the 15.79 M_{\odot} preSN progenitor and its consequently larger accretion rates during the 0.2-0.9 s period, as will be discussed in Section 5.4 with our discussion of the accretion luminosity. After 1.1 s, and particularly after 1.5 s, the gain region mass of F15.78 undergoes a surge and tends to exceed that of F15.79 for \approx 0.6 s, while that of F15.79 undergoes a surge after 1.65 s and tends to exceed that of F15.78 again for \approx 0.3 s, though the masses involved have become very small, $\sim 10^{-4} M_{\odot}$. These late surges in the gain region masses are associated with uptakes in the diagnostic and total energies and will be explored in Section 5.8.

The greater gain region mass, and therefore heating rate contribution in F15.79 from ≈ 0.2 –0.9 s arises from two factors: the larger (on average) density of the F15.79 gain region and its greater radial extent. Figure 13 illustrates the difference in the density profiles of the two models at 0.5 s postbounce. While the density is approximately the same at the base of the gain region for the two models, the figure shows that the density of F15.79 exceeds that of F15.78 as we move outward through the rest of the gain region and that the gain region of F15.79 extends well beyond that of F15.78. This is also evident in Figure 12, showing the gain radius and the radius enclosing

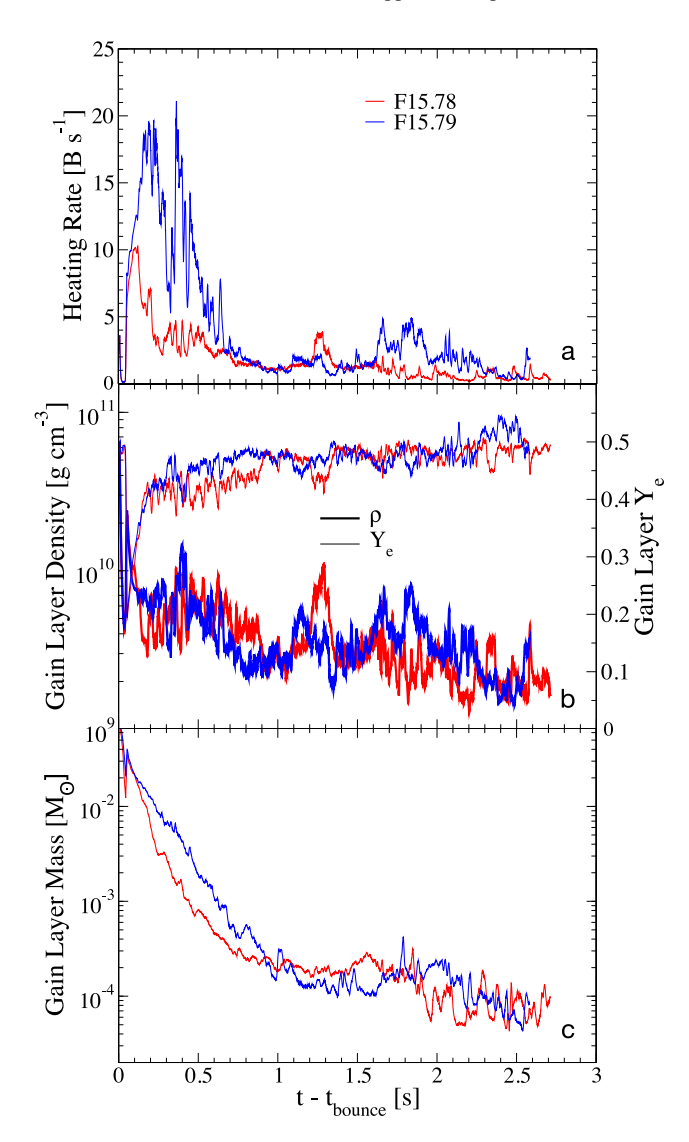


Figure 11. (a) neutrino heating rates, (b) density and the electron fraction in the gain layer, and (c) gain region mass.

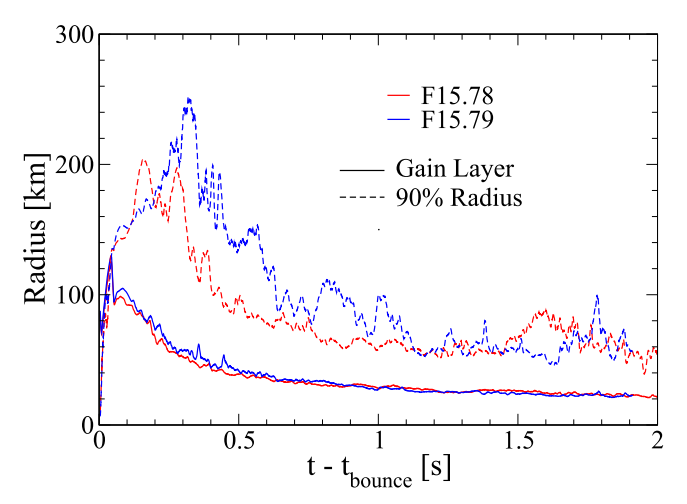


Figure 12. Gain layer radii, and radii enclosing 90% of the heating rate (smoothed).

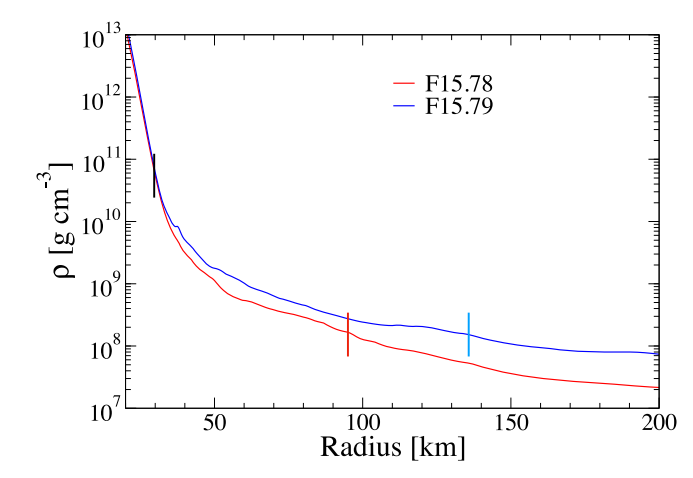


Figure 13. Density of the models against radius at 0.5 s postbounce. The black line segment locates the approximate radii of the ν_e and $\bar{\nu}_e$ neutrinospheres. The red and blue line segments mark the radius within which 90% of the heating rate is contained for F15.78 and F15.79, respectively.

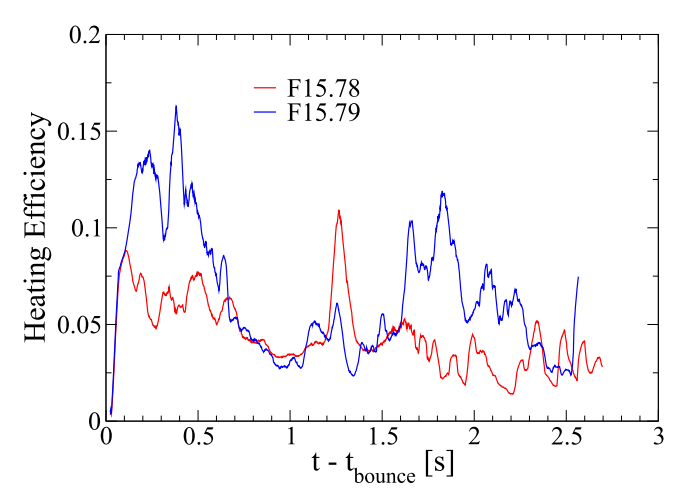


Figure 14. Neutrino heating efficiencies as defined by Equation (1).

90% of the neutrino heating rate. The density profile at 0.5 s is considerably flatter for F15.79 than for F15.78 with the density in F15.78 decreasing more rapidly with radius. This leads to a smaller heating region for F15.78 as follows from the radial dependence of the heating rate per unit radius, $\partial \dot{\mathcal{Q}}^+(r)/\partial r$ given by

$$\frac{\partial \dot{\mathcal{Q}}^{+}(r)}{\partial r} = 4\pi r^{2} \dot{q}^{+},\tag{4}$$

where \dot{q}^+ is the volume-specific heating rate given by Equation (3). The mean free paths in the heating region tend to be large and the neutrino luminosities in Equation (3) are therefore roughly constant across this region, which leads to $\dot{q}^+ \propto \rho/r^2$, where the $1/r^2$ factor is due to the radial dilution of the neutrino flux. Thus, the radial dependence cancels out and $\partial \dot{Q}^+(r)/\partial r$ scales with ρ , and the more rapid decrease of ρ with r in F15.78 results in its smaller thickness of the heating region.

A comparison that encapsulates most of the factors accounting for the differences in the heating rates between

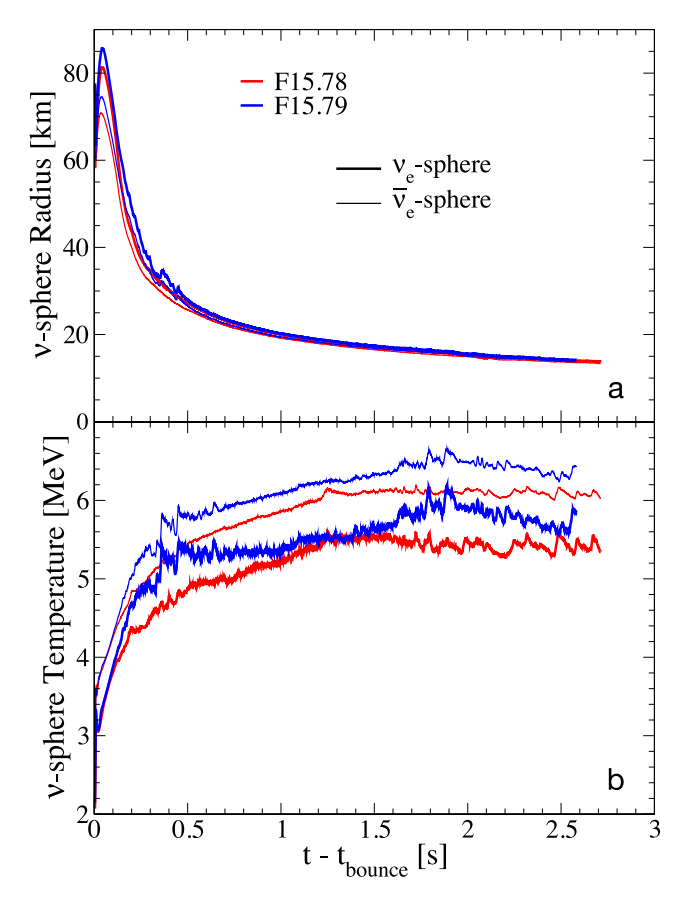


Figure 15. $\nu_e/\bar{\nu}_e$ neutrinopheric radii (a) and temperatures (b) as a function of postbounce time.

the two models is a comparison of their heating efficiencies, as defined by Equation (1) and plotted for the first 0.3 s in Figure 6 and for the full simulations in Figure 14. To the extent that the factors multiplying L_{ν_e} and $L_{\bar{\nu}_e}$ in Equation (3) are equal, the heating efficiency is just given by that equation without the factors L_{ν_e} and $L_{\bar{\nu}_e}$. Referring to Figure 14 in particular, it is clear that the heating efficiencies of F15.79 are factors of 2–3 times those of F15.78 in the critical 0.2–0.6 s period due to its larger RMS $\nu_e/\bar{\nu}_e$ energies and heating region mass. This reflects the corresponding differences in the heating rates, shown in Figure 11(a). Figure 14 also shows succeeding uptakes in the heating efficiencies of F15.78 at 1.2 s and 1.55 s and of F15.79 at 1.65 s. These are also associated with uptakes in the explosion energies and are discussed in Section 5.8.

We conclude that the primary causes for the differences in the heating rates for the two models are the differences in the ν_e and $\bar{\nu}_e$ luminosities and RMS energies, and the differences in the masses and density profiles of the gain regions. These in turn will be related below to the differences in the internal structures of the progenitors.

5.3. Neutrinospheres

The differences between the neutrino luminosities and RMS energies of the two models are related to differences in the geometric and thermodynamic conditions of their mean neutrinospheres, specifically, to the corresponding differences in their radii and temperatures. The use of mean neutrinospheres is an approximation, of course, but useful for a first-

order understanding of the differences in the neutrino luminosities and RMS energies between the two models.

Figure 15(a) plots the $\nu_e/\bar{\nu}_e$ -sphere radii. The $\nu_e/\bar{\nu}_e$ -sphere radii of F15.79 exceed those of F15.78 by as much as 5 km shortly after bounce, but thereafter diminishe to a couple of km at 0.25 s, and less than 1 km after 0.5 s. The nearly equal $\nu_e/\bar{\nu}_e$ -sphere radii, together with the nearly equal protoNS radii noted earlier, reflect, in part, the nearly constant mass–radius relation of the SFHo EoS for cold matter (Steiner et al. 2013). These initial differences in radii may explain the differences in the luminosities of the two models during the first several hundred ms, during which times their $\nu_e/\bar{\nu}_e$ -sphere temperatures (Figure 15(b)) are almost equal, but the $\nu_e/\bar{\nu}_e$ -sphere radius differences do not play a direct role in the $\nu_e/\bar{\nu}_e$ luminosity and RMS energy differences after that.

The near equality of the $\nu_e/\bar{\nu}_e$ -sphere radii of the two models does imply, however, that their luminosity and RMS energy differences are simply related. To the extent that Stefan's and Wien's laws (applied to fermions) are applicable here, the $\nu_e/\bar{\nu}_e$ luminosities are $\propto T^4$ while the RMS energies are $\propto T$. To first order, we therefore expect that

$$\frac{\mathrm{D}L_{\nu_e/\bar{\nu}_e}}{L_{\nu_e/\bar{\nu}_e}} = 4 \frac{\Delta E_{\nu_e/\bar{\nu}_e}}{E_{\nu_e/\bar{\nu}_e}},\tag{5}$$

where $\Delta L_{\nu_e/\bar{\nu}_e}$ and $\Delta E_{\nu_e/\bar{\nu}_e}$ are the $\nu_e/\bar{\nu}_e$ luminosity and RMS energy differences, respectively, between the two models. Referring to Figure 9, it is evident, despite the noise, that in the period from 0.2 s to 0.8 s, during which the differences in neutrino luminosity and RMS energy between the two models are significant, Equation (5) is approximately satisfied; likewise in the period from 1.65 s to 2.3 s. At other times, the luminosities and RMS energies are roughly similar. Our focus will now turn to the differences in the neutrino luminosities between the two models, keeping in mind the fact that the corresponding neutrino RMS energy differences are related to the neutrino luminosities differences as given approximately by Equation (5).

5.4. Distinguishing Core and Accretion Luminosities

To relate the differences in the $\nu_e + \bar{\nu}_e$ luminosities and RMS energies of the models to the differences in their progenitor structures, it is necessary, at least approximately, to separate from the total $\nu_e + \bar{\nu}_e$ luminosities, the component that emanates from the core (the core luminosity) and the component that arises from the energy released by recent mass accretion onto the protoNS surface (the accretion luminosity), as these components arise from different features of the progenitors. The accretion luminosity mirrors in time the radial density structure of the progenitor, and structural changes in the accretion streams as they affect the mass accretion rate onto the protoNS, while the core luminosity is governed more by the time integrated assembly history of the protoNS.

One measure of the $\nu_e + \bar{\nu}_e$ accretion luminosity, which we will denote by L_1 accrete, is given by the rate of kinetic energy accretion, namely

$$L_{1 \text{ accrete}} = \sum_{j, \nu_r < 0} \frac{1}{2} (\nu_r^2 + \nu_\theta^2)_{j, r = gain} \times \dot{M}_{j, r = gain},$$
 (6)

where, for each radial ray j, \dot{M}_{j,r_gain} is the rate of mass flow through the gain radius, and v_r and v_θ are the radial and angular

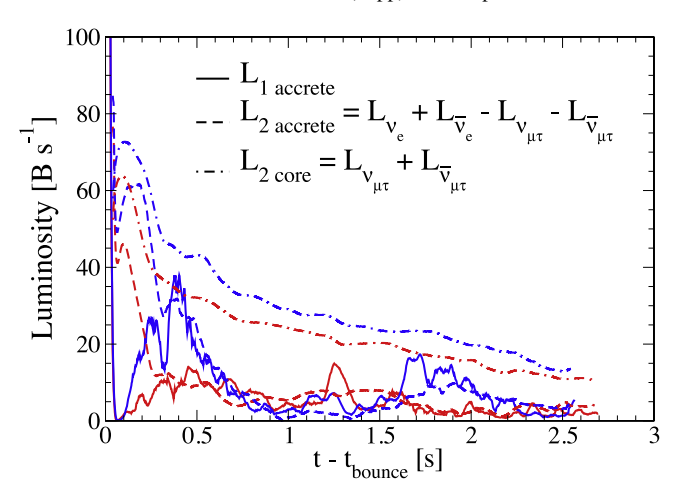


Figure 16. Accretion luminosity as defined by Equation (6) (solid lines), the accretion luminosity as defined by Equation (7) (dashed lines), and the core luminosity as defined by the sum of $L_{\nu_{\mu\tau}} + L_{\bar{\nu}_{\mu\tau}}$ (dotted–dashed lines), assuming that the core luminosities are the same for each neutrino flavor.

velocities at the gain radius, respectively. The sum is over all radial rays for which the fluid has negative radial velocities at the gain radius. We choose the gain radius to compute the rate of kinetic energy accretion as it is close to the surface of the protoNS and is most likely above the radius at which much of the flow is disrupted and thermalized. $L_{1 \text{ accrete}}$ for the two models is plotted by the solid lines in Figure 16.

An alternative scheme for distinguishing between the core and accretion $\nu_e + \bar{\nu}_e$ luminosities is to use the fact that, after the initial ν_e burst at shock breakout, the core luminosity of each neutrino flavor is approximately the same (Janka 1995). Given this, the $\nu_e + \bar{\nu}_e$ accretion and core luminosities, denoted respectively by L_2 accrete and L_2 core, are computed by

$$\begin{split} L_{\text{2 accrete}} &= L_{\nu_e} + L_{\bar{\nu}_e} - L_{\nu_{\mu\tau}} - L_{\bar{\nu}_{\mu\tau}}, \\ L_{\text{2 core}} &= L_{\nu_{\mu\tau}} + L_{\bar{\nu}_{\mu\tau}}, \end{split} \tag{7}$$

where, according to the above assumption, the sum of the ν_e and $\bar{\nu}_e$ core luminosities is given approximately by the sum of the $\nu_{\mu\tau}$ and $\bar{\nu}_{\mu\tau}$ luminosities, and the accretion luminosities are given by the difference between the total and the core luminosities (e.g., Müller & Janka 2014). Here $L_{\nu_{\mu\tau}}$ ($L_{\bar{\nu}_{\mu\tau}}$) refers to one of L_{ν} or L_{τ} ($L_{\bar{\nu}_{\mu}}$ or $L_{\bar{\nu}_{\tau}}$). L_{2} accrete as defined by Equation (7) is plotted in Figure 16 by the dashed lines, and the core luminosities as represented by the sum of the $\nu_{\mu\tau}$ and $\bar{\nu}_{\mu\tau}$ luminosities are plotted by the dotted–dashed lines.

Both methods of distinguishing accretion from core luminosities are only as good as the underling assumptions in their definitions. L_1 accrete assumes that the $\nu_e + \bar{\nu}_e$ accretion luminosity is given by the rate of kinetic energy accretion through the gain layer, and L_2 accrete suffers from its dependence on the assumption that the core luminosity of each neutrino flavor is the same, and from the numerically precarious procedure of obtaining the accretion luminosities by the subtraction of two large, comparably sized numbers. Despite their limitations, both methods of defining $L_{\rm accrete}$ agree rather well, with a few exceptions. Before 0.3 s, the $\nu_{\mu\tau}+\bar{\nu}_{\mu\tau}$ luminosity may be considerably smaller than the $\nu_e+\bar{\nu}_e$ core luminosity, invalidating the underlying assumption of their equality, and causing L_2 accrete to be much larger than L_1 accrete. Conversely, $r_{\rm gain}$ is large during this period

Table 1 Cooling Timescales ($\Delta t_{\rm cool}$) for the Indicated Layers in the ProtoNS for the Averaged Model

	$t - t_{\rm b} = 0.3 \text{ s}$	$t - t_{\rm b} = 0.5 \text{ s}$	$t - t_{\rm b} = 0.7 \text{ s}$
Shell (g cm ⁻³)		$\Delta t_{\rm cool}$ (s)	
10910	3.9×10^{-3}	2.0×10^{-3}	8.5×10^{-4}
10 ¹⁰¹¹	1.0×10^{-2}	3.4×10^{-3}	1.6×10^{-3}
10 ¹¹¹²	4.8×10^{-2}	1.3×10^{-2}	1.0×10^{-2}
10 ¹²¹³	2.9×10^{-1}	1.4×10^{-1}	1.1×10^{-1}

(Figure 12), and Equation (6) may be underestimating the kinetic energy inflow. Despite these discrepancies, both indicate that the core and accretion luminosities of F15.79 exceed those of F15.78 in the interval from 0.1 to 0.8 s, during which time most of the diagnostic energies of the models are acquired, and the differences between the models established. The differences between $L_{1 \text{ accrete}}$ and $L_{2 \text{ accrete}}$ after 0.3 s arise from 1.2 to 1.6 s in F15.78, where $L_{1 \text{ accrete}}$ exhibits several large fluctuations about $L_{2 \text{ accrete}}$, not seen in Figure 9, and from 1.65 to 2.0 s in F15.79, where L2 accrete exhibits several large peaks relative to L1 accrete, seen this time seen in Figure 9. These luminosity differences occur at the onset of accretion events (see Figure 18), where quantities are changing rapidly, and it may be that the direct relation between the inflow of kinetic energy and the accretion luminosity breaks down at these events. Despite their differences, both measures of the accretion luminosity increase during the above intervals, and are associated with uptakes in the explosion energy of the models, as can be seen in Figure 7(b). These accretion events and their effect on the explosion energy will be discussed in more detail in Section 5.8.

A further approach at distinguishing accretion from core luminosities, which we introduce below as an added corroboration of our above methods, utilizes the fact that the accretion luminosity is generated near the protoNS's surface where down-flows are shock terminated and partially thermalized while the core luminosity arises from the neutrino production and diffusion from deeper layers. We use the additional fact that the cooling timescales, which we define below, increase for successively deeper spherical regions in the protoNS when subjected to a given outflow of energy. These timescales are listed in Table 1, and are computed from

$$\Delta t_{\text{cool}} = \left(\frac{3}{2} k \frac{\Delta M}{m_{\text{B}}}\right) (L_{\text{in}} - L_{\text{out}})^{-1} \Delta T_{\text{cool}},\tag{8}$$

where ΔM is the mass of a given spherical region in the protoNS, $m_{\rm B}$ is the average neutron/proton mass, $L_{\rm in}-L_{\rm out}$ is the neutrino luminosity into minus the neutrino luminosity out of ΔM , and $\Delta T_{\rm cool}$ is a given change in temperature. The volume is assumed constant and the heat capacity assumes the nucleons behave like an ideal gas with negligible contribution from the partially degenerate electrons. In computing the cooling timescale entries of Table 1 from Equation (8), we have taken ΔM to be the mass of the spherical region enclosed between the indicated density limits, the net luminosity ($L_{\rm in}-L_{\rm out}$) to be -1 B s⁻¹, and $\Delta T_{\rm cool}$ to be -1 MeV. Both models provide similar values for ΔM in corresponding regions, and we have used the average of the two in the computation of the table entries. The fiducial times from bounce chosen to cover

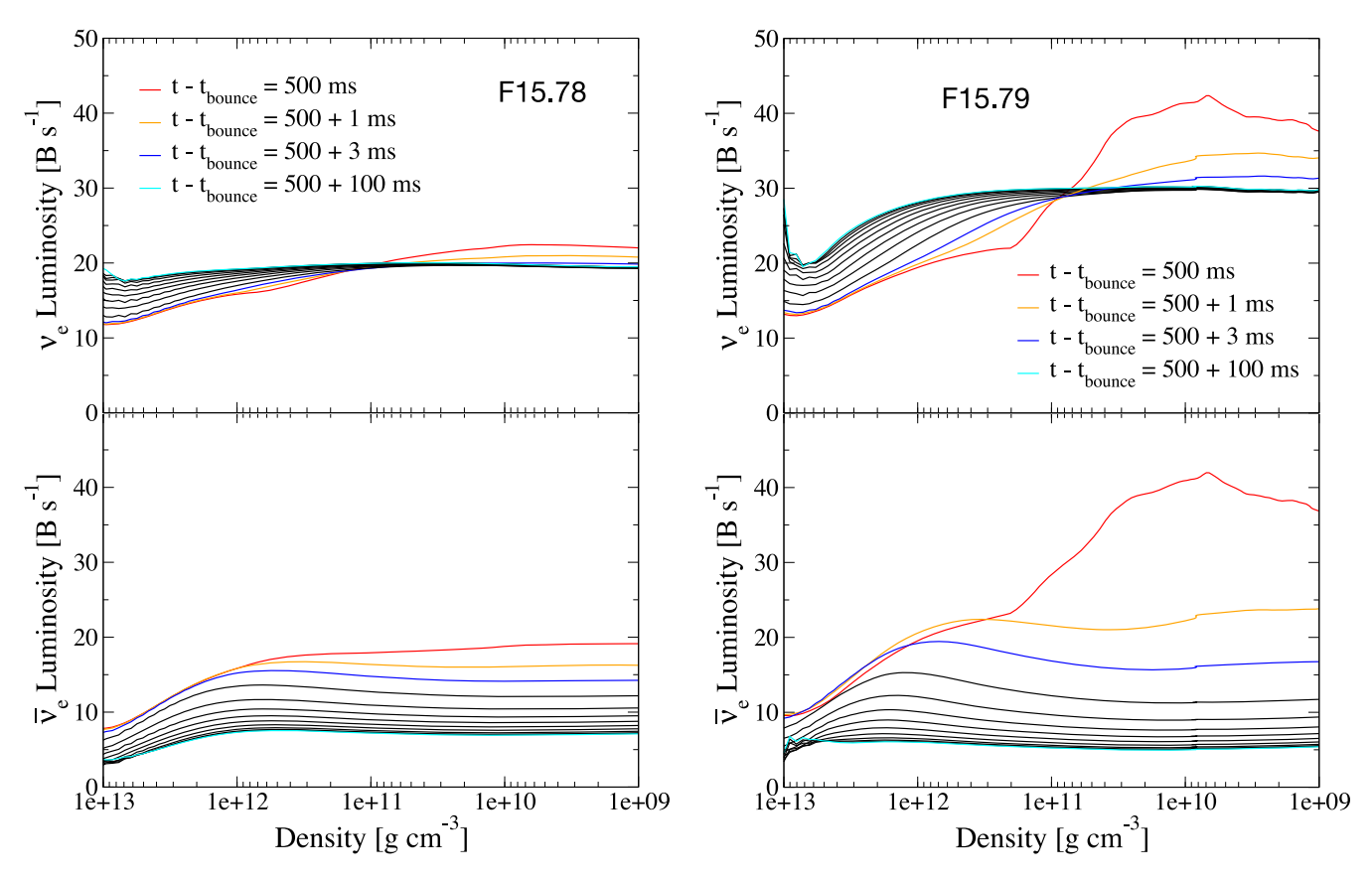


Figure 17. For F15.78 (left panels) and F15.79 (right panels), the upper and lower panels show snapshots of the ν_e and $\bar{\nu}_e$ luminosity, respectively, of the model at 500 ms by the red line. The orange, blue, and cyan lines show snapshots of the luminosities at the indicated times after 500 ms during which the hydrodynamics and Y_e were frozen. The black lines show the frozen hydrodynamic and Y_e luminosities from 10 to 90 ms in 10 ms intervals generated from the 500 ms initial configuration.

the period during which the bulk of the diagnostic energy of both models is acquired are 0.3, 0.5, and 0.7 s.

Given the cooling timescales listed in Table 1 for the conditions described above, distinguishing core from accretion luminosities at a given postbounce time, t_0 , can be accomplished, at least approximately, by taking as initial conditions the configuration of the model at time t_0 and continuing its simulation with the hydrodynamics and $Y_{\rm e}$ frozen, thereby eliminating the effects of accretion. With an appropriately chosen time interval $t - t_0$ for continuing the frozen hydro/ Y_e simulation, neutrino transport will quickly cool the accretion hot spots near the protoNS surface with their small cooling timescales, thereby eliminating the accretion luminosity, while transport from the deeper layers, with their much larger cooling timescales, will be largely unaffected. The luminosity remaining at the end of the above time interval should therefore be the core luminosity. Clearly this mode of separating core from accretion luminosities is not completely clean as there must be some overlap in their sources. It should provide semiquantitative results, however, which can be compared with the previous methods.

To determine values for $t-t_0$ that will be just sufficient to eliminate the effects of accretion, we have taken the spherical region in the protoNS between 10^{10} and 10^{11} g cm⁻³ as representative of the region where most of the accretion luminosity is generated. Values of $(L_{\rm in}-L_{\rm out})$ at time t_0 from this region turn out to be typically about -4 B s⁻¹ for F15.78 and about three times that in magnitude for F15.79. With these

values of $(L_{\rm in}-L_{\rm out})$ together with the timescale values of $\Delta t_{\rm cool}$ listed in Table 1 and computed with $(L_{\rm in}-L_{\rm out})=-1~{\rm B}~{\rm s}^{-1}$, we have chosen $t-t_0=3$ ms for both F15.78 and F15.79. This choice is further suggested by Figure 17, which plots snapshots of the ν_e and $\bar{\nu}_e$ luminosities at 0.5 s of the frozen hydro/ $Y_{\rm e}$ simulations, and the corresponding figures for the other fiducial times. These figures show that the ν_e luminosity ceases to change rapidly after 3 ms, indicating that the source of accretion luminosity has been radiated away, and furthermore that the $\bar{\nu}_e$ luminosity begins to decrease at densities above $10^{12}~{\rm g}~{\rm cm}^{-3}$ at 3 ms, indicating that the effects of the core luminosity are beginning to appear. From the results of these simulations at the fiducial times, the core and accretion luminosities as given by this procedure, and denoted by $L_{3~{\rm core}}$ and $L_{3~{\rm accrete}}$, respectively, are listed for both F15.78 and F15.79 in Table 2.

A comparison of the core and accretion luminosities, $L_{2 \text{ core}}$ and $L_{2 \text{ accrete}}$, given by Equation (7), with $L_{3 \text{ core}}$ and $L_{3 \text{ accrete}}$ is presented in Table 3 for the postbounce fiducial times of 0.3, 0.5, and 0.7 s. As in the definition of $L_{2 \text{ core}}$ and $L_{2 \text{ accrete}}$, each of the quantities $L_{3 \text{ core}}$ and $L_{3 \text{ accrete}}$ is the sum of the ν_e and $\bar{\nu}_e$ core and accretion luminosities, respectively. Several trends are evident from this table. First, for both F15.78 and F15.79, the core and accretion luminosities given by Equation (7) and by the frozen hydro/ Y_e simulations agree rather closely for $t-t_0=0.5$ and 0.7 s. On the other hand, at $t-t_0=0.3$ s the core and accretion luminosities given by Equation (7) are respectively smaller and greater than those given by the frozen hydro/ Y_e simulations. The origin of these differences is not

Table 2
Core and Accretion Luminosities

$t - t_{b}$ (s)	$L_{3 \nu_e \text{accrete}} \atop (\text{B s}^{-1})$	$(B s^{-1})$	$L_{3 \bar{\nu}_e ext{accrete}} (ext{B s}^{-1})$	$L_{3 \bar{\nu}_e \text{core} \atop S^{-1}}$
		F15.78		
0.3	3	25	6	18
0.5	3	20	5	14
0.7	4	15	6	15
		F15.79		
0.3	8	44	28	20
0.5	10	32	25	17
0.7	5	22	11	15

Table 3
Comparison of the Core and Accretion Luminosities

$t - t_{\rm b}$ (s)	$L_{2\text{accrete}}$ (B s ⁻¹)	L _{3 accrete} (B s ⁻¹)	$(B s^{-1})$	$(B s^{-1})$
		F15.78		
0.3	13	9	39	43
0.5	8	7	33	34
0.7	7	7	30	30
		F15.79		
0.3	48	36	51	64
0.5	34	35	47	47
0.7	15	16	38	37

clear, but a similar pathology was previously apparent in the comparison of $L_{1 \text{ accrete}}$ and $L_{2 \text{ accrete}}$ at early times, as shown in Figure 16, indicating the difficulty of separating core and accretion luminosities at these early times. Second, common to both methods of computing the core and accretion luminosities is the fact that the accretion luminosities are considerably smaller than the core luminosities during this time, and that both luminosities are larger for F15.79 than F15.78. A takeaway from the comparison of the L_2 and L_3 core and accretion luminosities is that the L_2 (and therefore the L_1) luminosities plotted in Figure 16 likely represent semiquantitatively the actual core and accretion luminosities for the models at times greater than 0.3 s. As noted above, for times less than 0.3 s it is likely that the assumption underlying Equation (7) is not valid and/or the accuracy of Equation (6) in accounting for the rate of kinetic energy infall at the radius where it is thermalized may be off. In the next two subsections we will attempt to account for these differences in the core and accretion luminosities between the two models, particularly for the period 0.12-0.8 s during which most of the diagnostic energy is acquired.

5.5. Accretion Luminosity Differences

A counterpart to the measure of the accretion luminosity $L_{1 \text{ accrete}}$, defined by Equation (6), is the rate of mass accretion itself, which is directly related to the density structure of the progenitor, mediated at later times by the progress of the shock. Figure 18(a) plots the in-flowing mass accretion rate, computed by summing over the mass accretion rates of all radial rays with negative radial velocities at the gain layer $r_{\rm gain}$. Figure 18(b) plots the net mass accretion rate through the same layer,

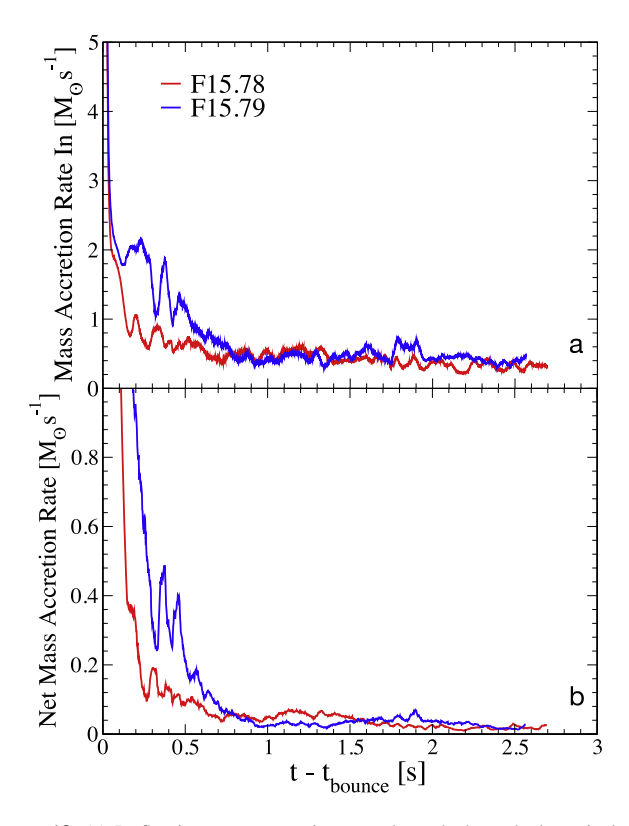


Figure 18. (a) In-flowing mass accretion rate through through the gain layer $r_{\rm gain}$ and (b) net mass accretion rate through the same surface defined as the inward minus the outward mass accretion rate.

defined as the in-flowing minus the out-flowing mass accretion rates. Both measures of the mass accretion rates show that the accretion rate for F15.79 substantially exceeds that of F15.78 for the period 0.12-0.8 s. This behavior of the accretion rates with time follows from the density profiles of the progenitors (Figure 4). The in-flowing rates for the two models (Figure 18(a)) are initially similar, but diverge at ≈ 0.12 s, when the density decrement of F15.78 reaches the vicinity of $r_{\rm gain}$. The earlier revival of the shock due to the density decrement further impedes accretion after this time in F15.78. The faster infall accretion velocities of F15.79 thereafter, due to the stronger gravity of its larger developing enclosed mass, cause the material at $r_{\rm gain}$ to originate from farther out, and therefore lower density, regions in the 15.79 M_{\odot} progenitor. This, in turn, causes its mass accretion rate to decline faster than that of F15.78 until the mass accretion rates of the two models become similar again at ≈ 0.8 s. We regard the net mass accretion rate (Figure 18(b)), which excludes matter that flows inwardly then outwardly, as the source of the accretion luminosity, as this excluded matter is presumed to deposit momentum hydrodynamically but none of its kinetic energy is assumed to be thermalized. Assuming nearly equal accretion efficiencies for the two models, the neutrino accretion luminosity originating from the mass accretion rate should roughly scale with these latter rates. We will refer to the accretion luminosity computed from the net mass accretion rate by $L_{\rm m}$ accrete.

A comparison of $L_{\rm m}$ accrete (Figure 18(b)) with $L_{\rm 1}$ accrete and $L_{\rm 2}$ accrete (Figure 16) shows that each measure gives similar qualitative descriptions of the accretion luminosities of the models when compared to each other. These relative accretion rates are correlated with the net $\nu_e/\bar{\nu}_e$ luminosity profiles

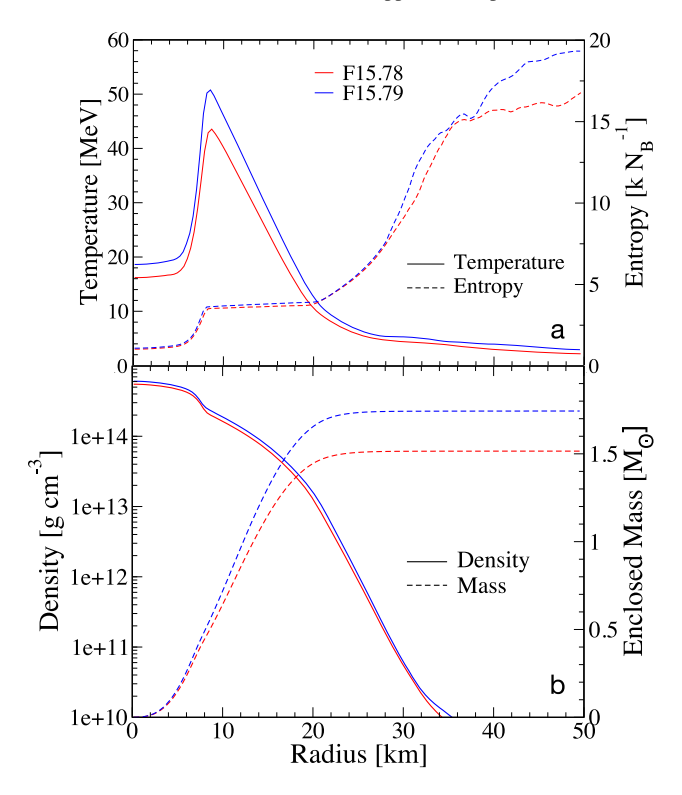


Figure 19. Structures of the model cores at 0.5 s postbounce: (a) the temperature and entropy of the models and (b) the density and enclosed mass of the two models

(Figure 9). Specifically, all accretion luminosity measures give values for F15.79 that are larger than F15.78 by a factor of 2–3, from about 0.12 to 0.6–0.8 s, during which time most of the diagnostic energy of the models is acquired. After 0.8 s, $L_{\rm m}$ accrete (Figure 18(b)) for F15.78 exceeds that for F15.79 from about 0.9 to 1.55 s, with the reverse being true from about 1.6 to 2.3 s. This is mirrored in the relative values of F15.78 versus F15.79 for both $L_{\rm 1}$ accrete and $L_{\rm 2}$ accrete (Figure 16), except that the values for F15.79 are higher relative to F15.78. The reason is that, the gain radii of the two models being nearly equal, (Figure 12) the larger mass of F15.79 interior to $r_{\rm gain}$ causes the kinetic energy of the infalling matter to be larger at $r_{\rm gain}$, thereby boosting $L_{\rm 1}$ accrete, which is related to the rate of kinetic energy infall, and $L_{\rm 2}$ accrete, which is based on the luminosities. In both cases, more energy is accreted and thermalized in F15.79 for the same accreted mass.

All measures of the accretion luminosity indicate that until about 0.8 s, the accretion luminosity is responsible for a significant fraction of the luminosity differences between the two models. This, in turn, contributes a significant fraction to the heating rate differences between the two models (Figure 11(a)). The accretion luminosity measures also exhibit broad accretion luminosity upturns initiated at 1.2 s for F15.78 and 1.65 s for F15.79, and these, along with the accretion luminosity peaks also exhibited in Figure 16, will be discussed in Section 5.8.

5.6. Core Luminosity Differences

Consider now the core luminosities. We first note that the differences in the core ν_e and $\bar{\nu}_e$ luminosities of the models may be inferred from those of $\nu_{\mu\tau}$ and $\bar{\nu}_{\mu\tau}$ as the latter species decouple from the matter deeper in the core and are less

affected by the accreted material at the protoNS surface. This, and the fact that the core luminosities of all neutrino flavors are approximately the same, led us to the core luminosity definition $L_{2\,\rm core}$ given by Equation (7) and plotted in Figure 16. Both the plots of $L_{2\,\rm core}$ for the models and the entries in Table 3 indicate that the core luminosities of F15.79 exceed those of F15.78.

These differences in core luminosities arise from the differences in the structures of the cores established $\sim 0.1 \text{ s}$ after bounce. Figure 19 plots the structures of the cores at 0.5 s postbounce. The low-entropy feature from the center to about 8 km is the cold inner core, resulting from the homologous, nearly adiabatic collapse of the inner part of the initial Chandrasekhar mass iron cores of the progenitors, the parts inside their respective sonic points, which have the same radius in both models. The inner core is surrounded by a warmer outer core that extends to ≈20 km, very nearly the same radius in both models, and is smoothed by protoNS convection. The mass of the F15.79 core at this time, however, is about 16% greater than the core of F15.78 as a result of the initial rapid mass accretion rate in the former; therefore, the core densities are about 16% greater in F15.79. As the additional compression of the F15.79 core due to the rapid mass accretion at its surface being isentropic, the core entropies are nearly the same in both models so that $T \propto \rho^{\gamma}$, with $\gamma \sim 1...3/2$ for a mixture of degenerate leptons and partially degenerate nucleons at constant entropy. (The EoS gives $T \propto \rho$ in this region). The temperatures in the two models exhibit a negative radial gradient extending from the inner-outer core boundary at ≈ 10 km (Figure 19(a)) for both models, to the neutrinospheres at ≈ 30 km (Figure 15(a)) for both models. The neutrino degeneracy parameter (μ_{ν}/kT) slowly varies along this interval, so neutrino transport should be dominated by energy rather than lepton transport, which can be crudely approximated by equilibrium diffusion

$$L = -4\pi r^2 \frac{7}{8} \frac{ac}{3} \ell \frac{dT^4}{dr} \qquad \ell \propto T^{-2} \rho^{-1}, \tag{9}$$

where ℓ is the mean free path and the factor 7/8 reflects fermion rather than photon transport. With the radial intervals the same for both models, and with $T \propto \rho$, and $\rho \propto M_{\rm core}$, we get that

$$L_{\rm core} \propto M_{\rm core}.$$
 (10)

Thus, the core luminosity scales approximately as M_{core} for our models and is therefore greater for F15.79 by about 16%. Integrating over the life of the protoNS, the core luminosity clearly dominates over the accretion luminosity (Figure 16). However, the periods of rapid growth in the explosion energy (0.12-0.8 s) coincide with the periods when the accretion luminosity most aggressively augments the core luminosity, especially in the F15.79 model. Mass accretion peaks and upturns (Figure 18) have disproportionately large effects on the explosion energy, as they not only increase the accretion luminosity, but also the density (Figure 11(b)) and mass (Figure 11(c)) of the gain region, and thereby the net neutrino energy deposition rate from both the core and accretion luminosities. One can therefore not ignore the contributions of recent accretion to the heating rate (Figure 11(a)) and the explosion energy (Figure 7) differences between these two models.

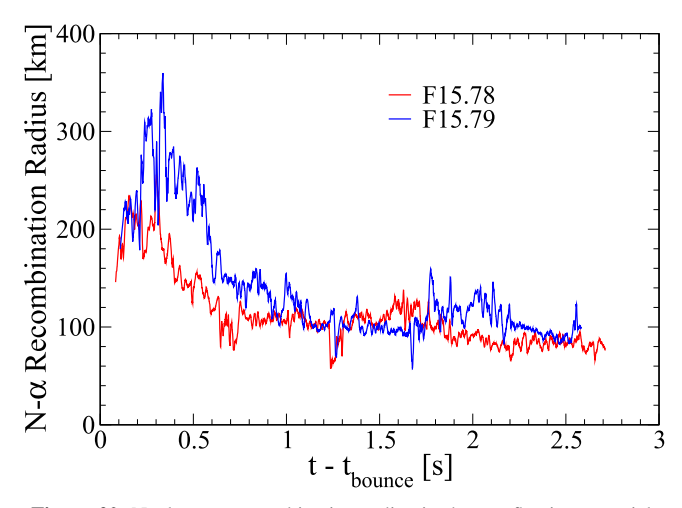


Figure 20. Nucleon– α recombination radius in the out-flowing material.

5.7. Outflows

We conclude our discussion of the important period 0.12–0.8 s where most of the diagnostic energy of the models was acquired with a brief look at the delivery of energy from the heating region to the shock. The larger neutrino heating rate for F15.79 relative to F15.78 (Figure 11(a)) leads to greater mass and energy ejected during the course of the explosion, as is evident from Figures 7(a) and (b). To examine this transfer of neutrino deposited energy to the shock, we set up (analogous to the approachs of Muller 2015; Bruenn et al. 2016) an ejecta volume, V_{ejecta} , with an inner radius, R_{ejecta} , at 400 km and an outer radius at the position of the shock, and consider matter with positive and negative radial velocities at $R_{\rm ejecta}$, i.e., matter flowing into and out of $V_{\rm ejecta}$, respectively, through the surface at $R_{\rm ejecta}$. The value of 400 km is chosen for $R_{\rm ejecta}$ because it lies outside the gain layer and most of the region where significant neutrino energy deposition is occurring (Figure 12), and outside the radius at which the recombination of nucleons to α -particles takes place (Figure 20). Partial recombination of α -particles into heavier nuclei does occur in $V_{\rm ejecta}$ for some of the matter, and that can add ~ 1 MeV baryon⁻¹ ($\sim 10^{18}$ erg g⁻¹) to the energy of the ejecta. Nuclear burning of shock-heated material adds little energy. The principle source of the diagnostic energy in V_{ejecta} is the enthalpy flow into V_{ejecta} through the R_{ejecta} surface.

In the following discussion, thermodynamic and other quantities associated with the up-flows at $R_{\rm ejecta}$ are taken as averages over the up-flow mass fluxes. That is, for a given specific mass quantity X, the flow rate of X into $V_{\rm ejecta}$ is given by

$$X = \sum_{j,u_j > 0} X_j \dot{M}_j / \sum_{j,u_j > 0} \dot{M}_j, \tag{11}$$

where X_j and M_j are the values of X and the mass flux of radial ray j at R_{ejecta} . Down-flow quantities are similarly defined.

Figure 21(a) shows the accumulated mass and enthalpy flowing into R_{ejecta} , where the enthalpy, h, is defined as

$$h = e_{\text{tot}} + p/\rho, \qquad e_{\text{tot}} = e_{\text{int}} + e_{\text{kin}} + e_{\text{grv}}, \qquad (12)$$

where $e_{\rm int}$, $e_{\rm kin}$, and $e_{\rm grv}$ are the baryon specific internal (not including rest mass), kinetic, and gravitational energies, respectively, and p is the pressure. The cumulative enthalpy input into $V_{\rm ejecta}$ is a measure of the diagnostic energy in that

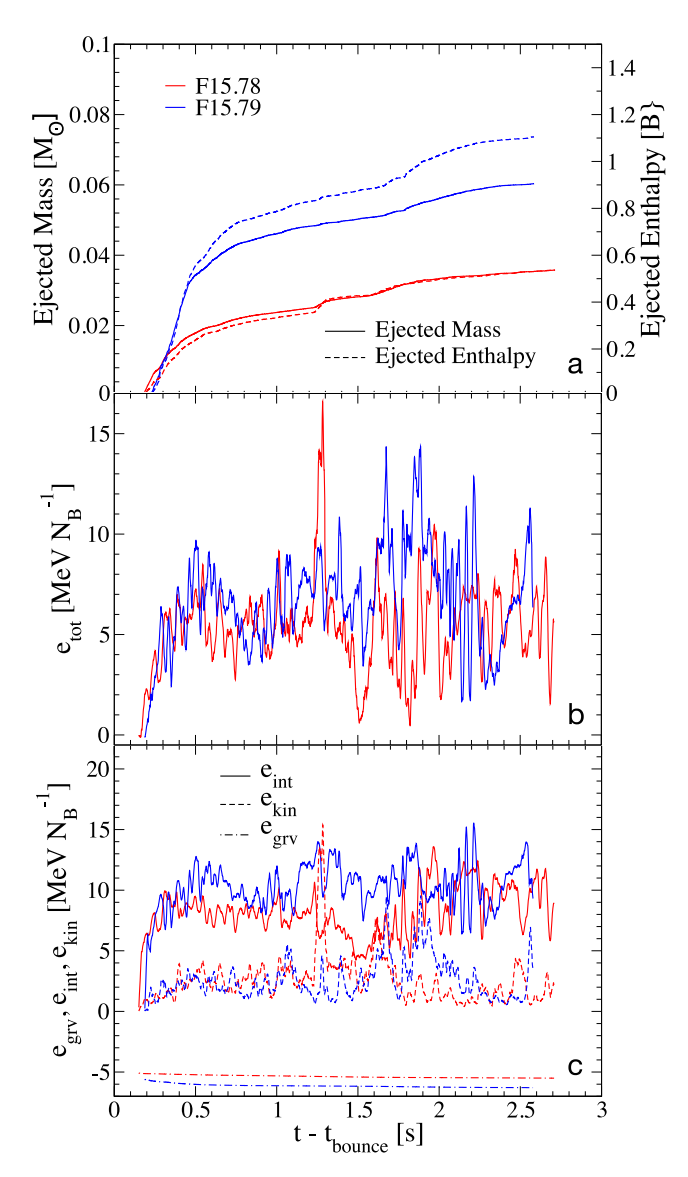


Figure 21. (a) Cumulative mass and enthalpy flows into $V_{\rm ejecta}$ through $R_{\rm ejecta}$, (b) total energy per baryon at $R_{\rm ejecta}$, and (c) components of the total energy per baryon at $R_{\rm ejecta}$.

volume, modulo recombination of α -particles into heavy nuclei, unbound material entrained in down-flows, and the upper moving boundary condition at the shock. Figure 21(a) shows that the cumulative mass flux into the ejecta region is larger for F15.79 than for F15.78, as to be expected, given its larger heating rate, but the difference in the cumulative enthalpy flux into the ejecta region is not proportional to the cumulative mass flux. To illustrate this, the enthalpy ordinate in Figure 21(a) is scaled so that the plot of cumulative ejected enthalpy lies on top of that for the cumulative ejected mass for F15.78. The cumulative enthalpy plot for F15.79, while initially coincident with its plot of cumulative ejected mass, begins at 0.5 s to deviate such that the cumulative total enthalpy to mass ratio is about 20% larger than in F15.78. This can be traced to the larger baryon specific total energy in F15.79 of the material at $R_{\rm ejecta}$ at these times, shown despite the noise in Figure 21(b). Examining the components of the total energy at $R_{\rm ejecta}$ shown in Figure 21(c), we note first that

the gravitational potential, $e_{\rm grv}$, is more negative for F15.79 than F15.78 as a consequence of its larger enclosed mass (Figure 8(b)). The baryon specific kinetic energies are about the same for the two models, but the internal energies are clearly different, being significantly larger for F15.79, overcompensating for its smaller gravitational energy, and accounting for its larger value of h at R_{ejecta} . Much of the internal energy acquired by rising fluid elements is from the recombination of free nuclei to ⁴He, and is approximately the same for both models. The greater internal energy acquired by a rising fluid element in F15.79 is due to its having been subjected to a more intense rate of neutrino heating and for a longer period, the former because of greater $\nu_e/\bar{\nu}_e$ luminosities and RMS energies for F15.79, and the latter because of the larger width of its gain region (Figure 12). The larger outflow of matter in F15.79 and the greater baryon specific enthalpy of this matter, both a result of its larger heating rate, results in a significantly greater rise in its explosion energy in comparison with F15.78.

5.8. Accretion Transients

We now briefly examine the diagnostic and total energy uptakes, initiated at 1.2 and 1.55 s for F15.78, and at 1.65 s for F15.79, as are manifested in Figure 7(b). These energy uptakes are caused by the corresponding mass accretion uptakes, with their proportionately large effects on the explosion energy (Section 5.6), together with accretion stream rearrangement transients. These are likely stochastic in nature and therefore not immediately related to differences in the internal structures of the progenitor models, which are the focus of this paper. Given that, we will provide only a brief account of these accretion transients.

5.8.1. F15.78

At 1.2 s, the overall shock geometry of F15.78 is similar to that at 1 s and is nearly unipolar, as shown in the bottom lefthand panel of Figure 10. At this time, the inward mass flow through r_{gain} increases (Figure 18), and a prominent accretion stream develops in the equatorial sector just to the north (right) of the equator with matter down-flows ultimately directed toward the vicinity of the protoNS from the northward direction. Immediately prior to 1.2 s, this accretion stream is encountering a standing accretion shock at a position approximately 20 km above the 20 km radius surface of the protoNS. This flow geometry changes after 1.2 s such that the standing accretion shock develops a cusp, allowing some of the preshocked material to reach the surface of the protoNS. This change in the mass accretion geometry is illustrated in Figure 22, where the protoNS is the blue (low entropy), semicircular figure at the bottom center, and the low-entropy mass accretion stream is the blue "tongue" at the upper right (a) and the center right (b). Note how the accretion stream has penetrated close to the surface of the protoNS in the interval from 1.15 to 1.25 s. This results in an increase in the accretion luminosity as computed by Equation (6) and displayed in Figure 16, as the standing accretion shock, originally above $r_{\rm gain}$ now falls below it. The accretion luminosity as computed by Equation (7) and shown in Figure 16 also responds to the change in the mass infall rate accretion geometry, but more gently. The altered mass infall rate and geometry also increases the gain layer density (Figure 11(b)), and ultimately the $\nu_e/\bar{\nu}_e$

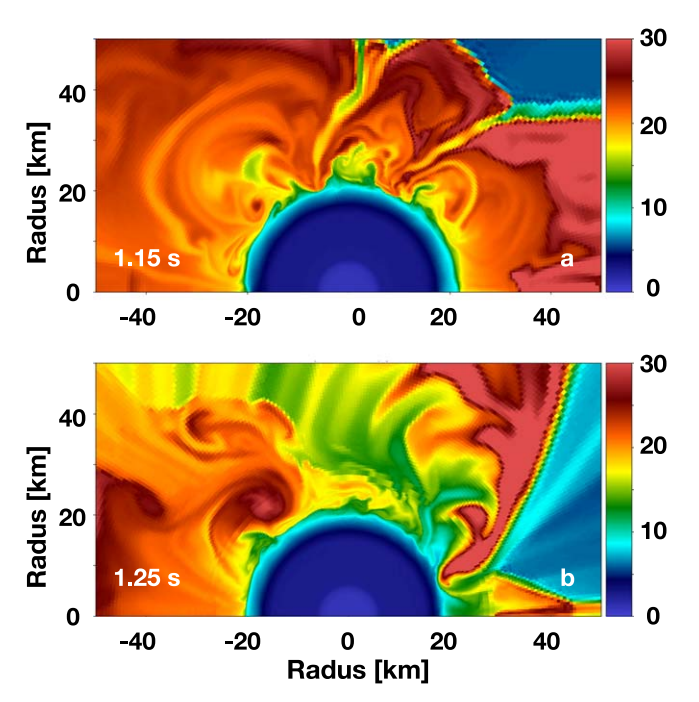


Figure 22. (a) Specific entropy of F15.78 at postbounce times of (a) $1.15 \, s$ and (b) $1.25 \, s$.

luminosities and RMS energies (Figure 9), resulting, in turn, in a subsequent increase in the heating rate (Figure 11(a)), and in the out-flowing mass and enthalpy rates (Figure 21(a)).

The energy uptake at 1.55 s also arises from the penetration of an accretion stream to the vicinity of the protoNS surface. In this case, the penetration is immediately preceded by a change in the direction of the accretion stream near the protoNS surface from being directed from the north to being directed from the south. The scenario producing an increase in the outflowing mass and enthalpy rates as a result of this change is similar to that described above for the energy uptake at 1.2 s, but more mild.

5.8.2. F15.79

The overall configuration of F15.79 at 1.65 s is similar to its configuration at 1 s, shown at the bottom-right panel of Figure 10. At 1.65 s, its configuration is highly prolate with several strong equatorial accretion channels, all of which swerve to the south of the protoNS, and are ultimately directed toward the vicinity of the protoNS from the south polar direction. Prior to 1.65 s, the accretion flow near the vicinity of the protoNS encounters an accretion shock located approximately 30 km above the 20 km radius surface of the protoNS, with a cusp near the southern edge of the flow through which a small amount of unshocked material penetrates to the vicinity of the protoNS surface. At 1.65 s, both accretion flows are joined and the accretion shock is pushed to within a couple of kilometers of the protoNS surface. This results in a near doubling of the mass accretion rate through r_{gain} (Figure 18(a) and(b)) that, when combined with the increased release of gravitational potential energy, results in a dramatic increase in the release of neutrino accretion luminosity, as reflected in the accretion luminosity displayed in Figure 16. The concomitent rise in the $\nu_e/\bar{\nu}_e$ RMS energies (Equation (5) and Figure 9) and the increase in the density of the gain region (Figure 11(b)) combine to at least double the neutrino heating efficiency

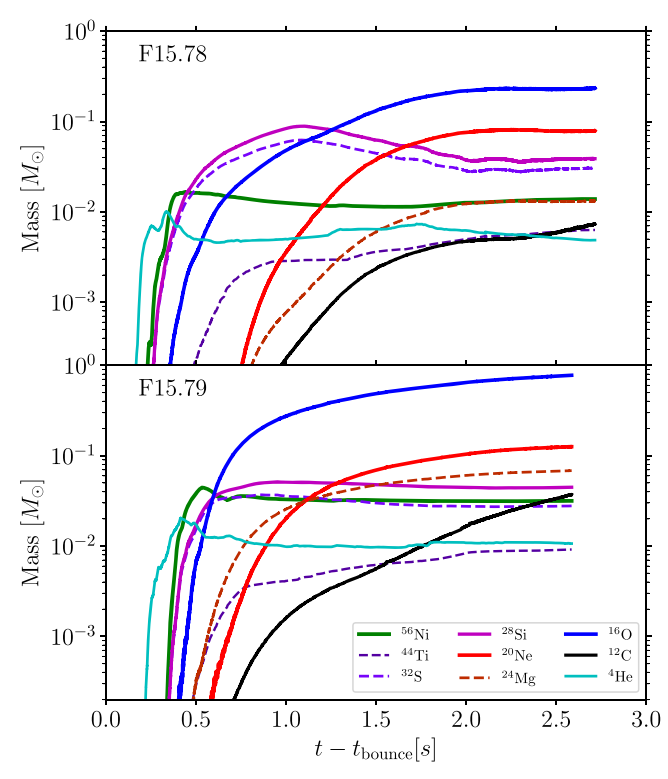


Figure 23. Time evolution of the unbound mass of the most important nuclear species in the α -network for F15.78 (top) and F15.78 (bottom).

(Figure 14). The increases in the heating efficiency, neutrino luminosity, and RMS energy increase the heating rate (Figure 11(a)) by several, and the rates of mass and enthalpy ejected (Figure 21(a)), resulting in the uptake in the explosion energy.

6. Nucleosynthesis

The small anp56 nuclear reaction network included within these simulations is not suitable to give accurate nucleosynthesis predictions but we can use the approximate abundances it provides to illustrate the impact of the differences in the stellar structure of the two models has on the composition of the ejecta. Harris et al. (2017) have discussed the caveats of small reaction networks for nucleosynthesis predictions, but found that the yields of the most common isotopes, including $^{56}\rm Ni, ^{28}\rm Si,$ and $^{16}\rm O$ are relatively well reproduced by an α -network, while deviations can be large for $^{44}\rm Ti.$ What is important for this analysis is the relative outcomes between the models that parallel some of the features of the explosion dynamics discussed in Section 5 and the differences in the progenitor composition.

6.1. Isotopic Yields

In Figure 23 we show the evolution of the composition of our estimated ejecta defined as the material contained in all zones with a positive total energy (thermal + kinetic + gravitational). This mirrors the diagnostic energy (Figure 7). In both simulations, the first material to become unbound is very hot and consists mainly of free nucleons and α -particles. Afterwards, ⁵⁶Ni appears from both the freeze out of NSE and explosive Si burning as the shock progresses through the Si shell. Unburnt ³²S and ²⁸Si become unbound afterwards, as incomplete Si burning, followed by O burning occur in the

shock. ⁴⁴Ti appears with some delay from the α -rich freeze out of high-entropy ejecta. When the shock leaves the Si shell, ¹⁶O, ²⁰Ne, and ²⁴Mg, and eventually ¹²C, join the ejecta, reflecting mostly the ejection of the progenitor's composition. The formation of accretion downstreams, which can also entrain part of the previously unbound material, causing it to fall back, is reflected in the decrease of the unbound ⁵⁶Ni and especially ²⁸Si/³²S masses. Explosive Si burning is completed in both models at the end of the simulation and the unbound masses of ²⁸Si/³²S and ⁵⁶Ni have stabilized. The ongoing increases of ¹⁶O and ¹²C show the shock ejecting the O/Ne and C shells without inducing significant nuclear reactions. Qualitatively, these features are common to both models discussed here, and other CCSN simulations (see, e.g., Bruenn et al. 2016; Harris et al. 2017; Eichler et al. 2018; Sieverding et al. 2020), but the details reflect important differences between the models.

⁵⁶Ni yield—due to the rather weak and very asymmetric explosion of F15.78, most of the ⁵⁶Ni is produced in the direction where the explosion is strongest in a relatively narrow cone along the axis. Most of this ⁵⁶Ni, created by explosive Si burning in F15.78, is ejected unhindered with only a gradual decrease in the unbound mass visible in Figure 23 reflecting ongoing accretion. A slight boost in ⁵⁶Ni accompanies the boosts in explosion energy after 1.2 s (see Figure 7) as more matter joins the ejecta. In the other directions, where the explosion is weaker, there is little Si burning. In F15.78, the unbound ⁵⁶Ni mass reaches its peak at about 400 ms, which is earlier than the peak in ⁵⁶Ni for F15.79 at around 550 ms. This also reflects the slightly delayed shock expansion in F15.79 (see Figure 7). F15.79 exhibits a higher overall accretion rate (see Figure 5) and associated accretion luminosity early on that causes a significant amount of the initially formed ⁵⁶Ni to fall back, leading to the more pronounced peak at 550 ms.

At the end of the simulation, there is $1.4 \times 10^{-2} M_{\odot}$ of 56 Ni unbound for F15.78 compared to $3.2 \times 10^{-2} M_{\odot}$ in F15.79. Observationally, this also implies that the explosion of a star similar to the progenitor of F15.78 would appear much dimmer than a star similar to F15.79. The higher 56 Ni yield and 2.5 times higher explosion energy in F15.79 follows the strong correlation between the explosion energy and the production of 56 Ni seen in observations (see, e.g., Martinez et al. 2022). As discussed in Section 2, the 15.79 M_{\odot} preSN model has higher compactness than the 15.78 M_{\odot} preSN model, correlating with the higher 56 Ni yields in F15.79, agreement with the finding of Ebinger et al. (2019), for neutrino-driven, spherically symmetric explosions, that higher compactness correlates with higher 56 Ni yields.

⁴⁴Ti yield—the amount of ⁴⁴Ti is overestimated by the anp56 reaction network by roughly an order of magnitude (Harris et al. 2017) compared to the results of more realistic reaction network; therefore, its value should be considered to represent a broader composition of species resulting from α-rich freeze out from NSE. The numbers quoted here should therefore be compared directly to observations with care. In both simulations, ⁴⁴Ti is first produced at the edge of the initial, high-velocity blast that ejects hot material from the Fe core as free nucleons and α-particles. When this material expands into the O shell and rapidly cools, ⁴⁴Ti forms. This leads to the increase in unbound ⁴⁴Ti between 400 ms and 700 ms visible in Figure 23 for both simulations. Note this is ~200 ms after the rise of ⁵⁶Ni. About 45% of the final ⁴⁴Ti mass becomes unbound during this phase, less than 1 s after bounce.

Additional ⁴⁴Ti is produced later in the high-entropy, neutrinoheated material. For example, Figure 23 shows an increase in the unbound α -particle mass in F15.78 at \sim 1.3 s after bounce that is associated with the increase of the heating rate (see Section 5.8.1 & Figure 11(a)). This outburst of neutrino heating drives an outflow from the region near the protoNS that then undergoes an α -rich freeze out as it expands. More than half of the final ⁴⁴Ti yield in F15.78 only forms after this event, in the freeze out of the neutrino-heated material. The evolution of the ⁴⁴Ti mass for F15.79 (lower panel of Figure 23) is more smooth, but is also shows episodes of increased ⁴⁴Ti formation at about 1.3 s and 1.8 s, which are associated with the episodes of increased heating shown in Figure 11 (see Section 5.8.2). Since ⁴⁴Ti results from an α -rich freeze out from NSE, the unbound mass of ⁴He shows similar features.

At the end of the simulations, we find ejected masses of $6.3 \times 10^{-3}~M_{\odot}$ of 44 Ti for F15.78 and $9.2 \times 10^{-3}~M_{\odot}$ for F15.79. It is interesting to note that the unbound mass of 44 Ti does not scale in the same way with the explosion energy as 56 Ni. As a consequence, the 44 Ti/ 56 Ni mass ratio is higher in F15.78 (0.45) than in F15.79 (0.29). Due to the very low explosion energy of F15.78, it is likely that a significant fraction of the 44 Ti produced at late times may eventually fall back onto the NS. A clear assessment of the nucleosynthesis yields of this model requires following the explosion to much later times.

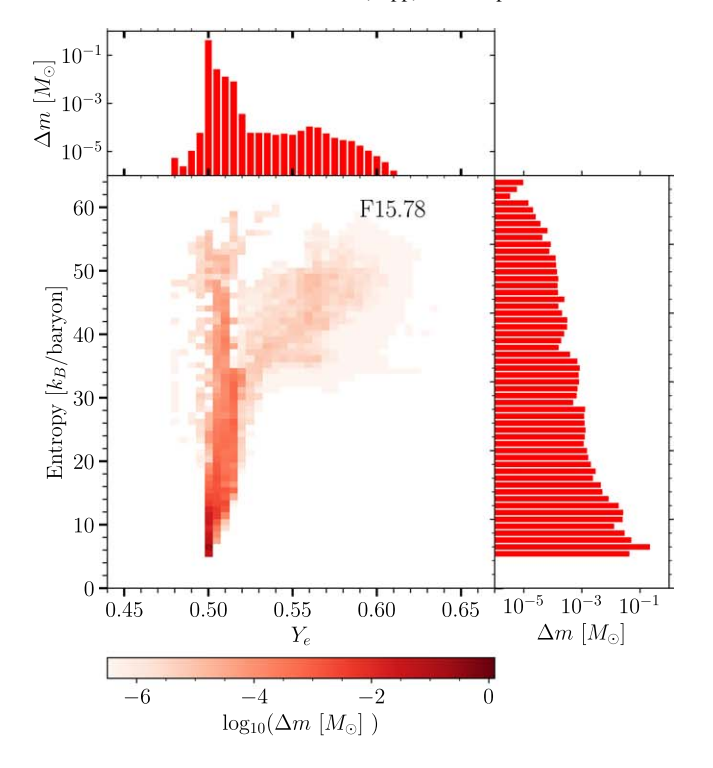
²⁸Si and ¹⁶O yields—the lower compactness and smaller core of the 15.78 M_{\odot} progenitor model and the stronger explosion of F15.79 have a significant impact on the evolution of ¹²⁸Si in the ejecta. Overall, the 15.78 M_{\odot} preSN model contains 0.86 M_{\odot} of ²⁸Si, which is slightly more than the 0.79 M_{\odot} of ²⁸Si in the 15.79 M_{\odot} preSN model. In the 15.79 M_{\odot} preSN model, the Si core is much more compact and only 0.18 M_{\odot} of ²⁸Si is found outside of the NSE region at collapse, compared to 0.28 M_{\odot} of ²⁸Si in the 15.78 M_{\odot} preSN model. In the 15.78 M_{\odot} preSN model, the Si-rich layer is also very extended in radius, reaching out to almost 8000 km (Figure 3). It takes almost 1 s for the average shock radius in F15.78 to reach the O shell. A large amount of ²⁸Si becomes unbound without being burnt reaching more than $0.1 M_{\odot}$ at around 800 ms after bounce. At its peak, the amount of unbound ²⁸Si is one order of magnitude larger than the unbound ⁵⁶Ni mass. As the unipolar morphology of F15.78 is established, the strong and persistent accretion stream captures more than half of the temporarily unbound ²⁸Si from the progenitor's Si shell. For the 15.79 M_{\odot} progenitor, on the other hand, the Si shell is more compact, extending only to about 3,000 km and the shock leaves the Si shell only 600 ms after bounce. As a consequence, a larger fraction of ²⁸Si is burnt to ⁵⁶Ni, such that the difference between unbound ²⁸Si and ⁵⁶Ni remains much smaller than in the F15.78 model.

While the ⁵⁶Ni mass is very different between the two simulations, the ejected ²⁸Si mass is more similar, with $3.9 \times 10^{-2} M_{\odot}$ for F15.78 and $4.5 \times 10^{-2} M_{\odot}$ of ²⁸Si for F15.79. This leads to a much larger ²⁸Si/⁵⁶Ni mass ratio in F15.78. The larger final yield of ²⁸Si for F15.79, which is based on the progenitor model with less ²⁸Si at collapse, is a sign of stronger explosive O burning in the F15.79 model due to the more-energetic shock compared to the F15.78 model. Figure 3 also shows that most of the Si shell of the 15.78 M_{\odot} preSN model contains at least 10% ¹⁶O. Consequently the unbound mass of ¹⁶O also increases gradually as ²⁸Si is swept up by the shock in

F15.78. This also reflects the relatively weak shock, which does not allow for a significant amount of explosive O burning. In the 15.79 M_{\odot} progenitor, on the other hand, the Si shell is free of 16 O and it becomes unbound more abruptly once the shock has reached the O shell. The large difference in the amount of unbound 16 O at the end of the simulation is partly due to the morphology of the explosion in F15.78, where most of the unbound 16 O is ejected in the narrow cone where the explosion is strongest, while a large fraction of the O shell and C shell remain undisturbed and thus are not unbound at the end of the simulation. In order to determine the final yields of 16 O and 12 C, the simulation needs to be continued to even later times, since the usual assumption that the shock will successfully eject the remainders of these layers seems suspect in this highly aspherical, weakly exploding case.

 20 Ne and 24 Mg yields—the ejection of 20 Ne and 24 Mg also reflects the progenitor structure. Figure 3 shows that there is 24 Mg at the bottom of the O-burning shell between about 3–4000 km in the 15.79 M_{\odot} preSN progenitor, where 20 Ne has been burnt. As a consequence, in F15.79, 24 Mg appears in the unbound material before 20 Ne. For F15.78, both 20 Ne and 24 Mg start to be unbound at about the same time when the maximum shock radius reaches 10,000 km—the edge of the O shell containing 20 Ne and 24 Mg. Since 24 Mg is about one order of magnitude less abundant than 20 Ne in the preSN model, the 24 Mg mass in the ejecta increases much more slowly.

Comparison to other models—while the focus of this study is on the differences between two models based on stellar progenitors with almost identical masses, we briefly discuss our results in the context of other models from the available literature. We focus on ⁵⁶Ni because it is most commonly reported and we expect a reasonable estimate from our small α network. Postprocessing parametrized explosions in spherical symmetry with a large reaction network, Curtis et al. (2019) find much higher yields for 56 Ni for stellar models of comparable initial masses, e.g., $9.86 \times 10^{-2} M_{\odot}$ for a 15.8 M_{\odot} progenitor model and $7.54 \times 10^{-2} M_{\odot}$ for a 16.0 M_{\odot} progenitor model, both from Woosley et al. (2002). They also find $6.64 \times 10^{-2} M_{\odot}$ of ⁵⁶Ni for a 16 M_{\odot} progenitor model from Woosley & Heger (2007). These higher yields are consistent with the higher explosion energies, larger than 10⁵¹ erg, obtained with their spherically symmetric parameterization (Ebinger et al. 2019). The differences in the yields from models with similar initial masses and from slightly different versions of the same stellar evolution code illustrate a general sensitivity to the progenitor structure that is, in relative terms, comparable to the differences we find here. It remains, however, unclear whether the origins of these differences are the same. The ⁵⁶Ni yield of F15.79 is close to the value of 0.038 M_{\odot} estimated by Bollig et al. (2021) based on a 3D simulation of a 19 M_{\odot} progenitor that also employs an α -network. Eichler et al. (2018) have also noted very low ⁵⁶Ni yields based on long-term axisymmetric simulations extended to more than 5 s after bounce and a strong sensitivity to the ejection criterion. These authors find a range from 9.5×10^{-3} to $6.6 \times 10^{-2} M_{\odot}$ of ⁵⁶Ni for their 17 M_{\odot} model depending on the ejection criterion and argue that a large amount of ⁵⁶Ni is eventually accreted. While we find yields that are higher than the values reported by Eichler et al. (2018), the simulations need to be run longer to clarify which material is eventually ejected.



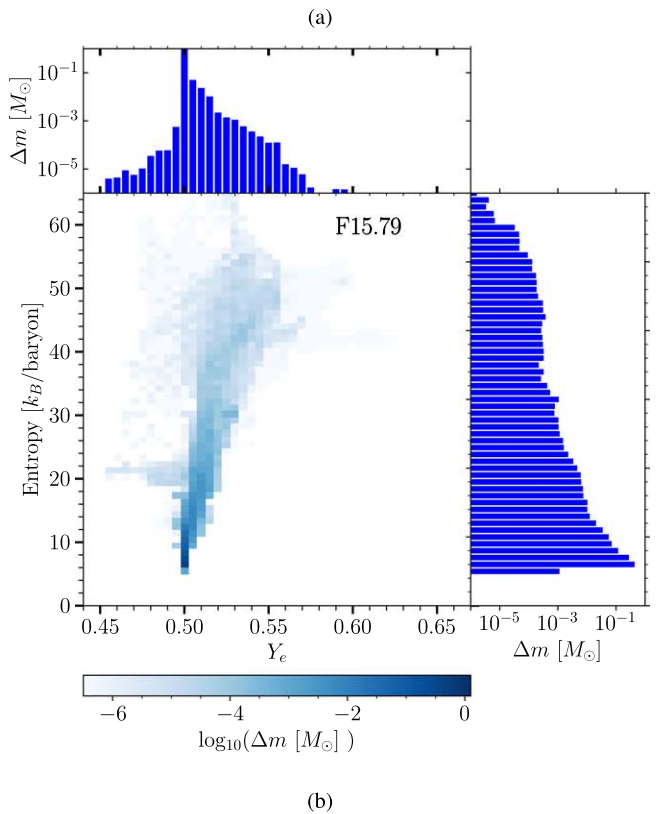


Figure 24. Distributions of Y_e and entropy of unbound matter at the end of the simulations for (a) F15.78 and (b) F15.79.

6.2. Entropy and Ye Distributions

More than 15,000 passive Lagrangian tracer particles have been included in each simulation that will be postprocessed with a large nuclear reaction network for detailed nucleosynthesis yields in future work. To assess the possibilities for neutron- and proton-rich nucleosynthesis of heavier elements, Figure 24 shows the distributions of Y_e and entropy for the unbound material at the end of each simulation.

In both simulations, the unbound material is mostly proton rich $(Y_e > 0.5)$, with Y_e ranging from 0.48 to 0.61 for F15.78 and from 0.46 to close to 0.60 for F15.79. Most of the material that is just swept up by the shock stays at values of $Y_e \approx 0.5$ and entropies below $15 k_{\rm B}$ baryon⁻¹. The distribution for F15.78 is particularly narrow, with the vast majority of the ejecta centered around $Y_e \approx 0.5$ but a relatively long tail of high Y_e . This can be understood as a consequence of the early, but relatively weak explosions, with low neutrino heating rates described in Section 5. The explosion of F15.79 experiences more neutrino heating (Figure 11) and consequently shows more material with $Y_e > 0.5$. As noted by Wanajo et al. (2018), there is a general correlation between high entropy and high Y_e because neutrino exposure tends to increase both quantities. The distributions in Y_e shown in Figure 24 are much narrower than the results presented by Wanajo et al. (2018), but they report the value of Y_e at freeze out, rather than at the end of the simulation, which does not allow a direct comparison.

There are two noticeable features that merit further discussion. First, it is unexpected to find the most proton-rich material in F15.78, which exhibits a lower explosion energy and, on average, less-energetic neutrino emission. From the distribution in Y_e -entropy space in Figure 24(a), it is clear that the highest- Y_e material branches off from the bulk of the ejecta. Closer inspection shows that the high- Y_e material is part of a plume that develops at around 1.7 s after bounce in the direction opposite to the unipolar explosion, i.e., to the right in Figure 10. The material expands rapidly along the symmetry axis as it is pushing against the weakening downstream that moves away from the axis. Strong neutrino heating results in high Y_e and significant entropy. Comparing these conditions to the results presented by Xiong et al. (2020), we anticipate a small contribution to the lighter p-nuclei up to ⁷⁸Kr. Because of the higher neutrino luminosity in F15.79 relative to F15.78, it is surprising that F15.78 reaches higher values of Y_e . This is connected to the unusual unipolar morphology of the F15.78 explosion and probably affected by the assumption of axial symmetry, which favors the development of the outflow along the axis. Due to the marginal explosion in this model, it is not clear whether a significant fraction of this material would eventually become part of the ejecta. While F15.78 reaches unexpectedly high values of Y_e , very little mass is ejected under such conditions. The total mass of material with $Y_e > 0.5$ is larger for F15.79, almost 0.1 M_{\odot} , compared to only 0.02 M_{\odot} of proton-rich ejecta in F15.78.

The second noticeable feature is the neutron-rich material in F15.79 with a distribution extending down to Y_e of nearly 0.45 and an entropy of around $20 k_{\rm B}$ baryon⁻¹. This material is part of an outflow that forms at around 1.9 s after bounce, when the dominant accretion streams start to shift from a position close to the equator to one side of the protoNS. The formation of the downstream and the resulting increase of the density make the neutrinosphere on that side of the protoNS move outward, reducing the average neutrino energies. Most of the material in this downstream is accreted onto the protoNS, but a small fraction of the material gets compressed against the symmetry axis and is ejected in a cone along the axis without getting close to the protoNS and without strong neutrino exposure. Since the neutrino energies on that side of the protoNS are relatively low

due to the increased density and the material never gets very close to the protoNS, Y_e remains low due to electron captures when compressed against the axis. This outflow is also probably exaggerated by the 2D nature of the simulation, which allows the down-flow to be deflected by the axis. While the conditions of this material are interesting for the nucleosynthesis of elements heavier than Fe, the total mass of unbound material with $Y_e < 0.47$ is less than $3.5 \times 10^{-5} M_{\odot}$, satisfying the constraint that CCSNe should not eject more than $10^{-4} M_{\odot}$ of material with such low Y_e in order to prevent the overproduction of certain heavy elements (Hoffman et al. 1996). A detailed analysis with tracer particles is necessary to determine the potential contribution of this type of material to chemical evolution. We note that similar ejecta with Y_e as low as 0.4 and $S \approx 15 k_{\rm B} \, {\rm baryon}^{-1}$ have been found previously in 2D CCSN simulations presented by Wanajo et al. (2018) for a 27 M_{\odot} progenitor model.

The appearance of individual outflows with conditions that are interesting for the nucleosynthesis of heavy elements very late in the simulation emphasizes the need to run long-term SN simulation that capture the conditions of these low-mass outflows. The emergence of these features is the result of chaotic fluid flows, rather than a direct effect of differences in these progenitor models. However, the overall accretion rate, which is governed by the interplay of the progenitor structure and the developing explosion, does impact the appearance and evolution of outflows like these.

7. Summary and Conclusions

Recent stellar evolution modeling of massive stars (Sukhbold et al. 2018) has indicated a bimodal variability, related to specific patterns of shell-burning interactions, which can result in two nearly equal ZAMS mass progenitors ending up with significantly different internal structures at the time of CC. To explore the implications of this bimodal variability for CC and subsequent evolution, we have followed the CC evolution in 2D for almost 3 s of two nearly equal-mass progenitors, 15.78 and 15.79 M_{\odot} , with different internal structures as detailed in Section 2. Shock stagnation after bounce occurs in both models at approximate 160 km. The 15.78 M_{\odot} progenitor exhibits a substantial density drop at the S/Si-O composition interface resulting in significant drop in the accretion ram pressure for F15.78 when that interface arrives at the shock front, approximately 120 ms after bounce. This caused a strong shock expansion which, in turn, triggered runaway conditions for an explosion. With no strong density decrement characterized in its progenitor, the explosion for F15.79 sets in 100 ms later than in F15.78 due to a gradual decrease in the accretion ram pressure at the shock front together with hardening of the neutrino energy spectra and a corresponding increase in the neutrino heating efficiencies. Despite the early shock revival of F15.78, more neutrino energy is deposited into the heating region of F15.79 and the shock of the latter rapidly overtakes that of F15.78. By the end of the simulations, the diagnostic energy of F15.79 is \approx 0.74 B and that of F15.78 is \approx 0.26 B.

The more powerful shock and greater energetics of F15.79 that arise during the 0.2–0.8 s postbounce period can be traced ultimately to the more massive ($M_4=1.78~M_{\odot}$ versus 1.47 M_{\odot}) and denser core of its progenitor. The immediate consequence of this is a larger mass accretion rate during the 0.2–0.8 s epoch, giving rise to a greater $\nu_e/\bar{\nu}_e$ accretion luminosity and a denser and more extended gain region. At the same time, the

added accumulated mass on the F15.79 inner core supplied by the larger mass accretion rate forces the core to undergo a greater adiabatic compression and a resulting higher peak temperature, leading to a greater $\nu_e/\bar{\nu}_e$ core luminosity. Since the $\nu_e/\bar{\nu}_e$ luminosities of both models emanate from neutrinospheres of approximately the same radii, the greater $\nu_e/\bar{\nu}_e$ accretion and core luminosities in F15.79 result in greater $\nu_e/\bar{\nu}_e$ RMS energies. Finally, the greater $\nu_e/\bar{\nu}_e$ luminosities and RMS energies in F15.79 and the more massive and flatter density profile of its gain region lead to a substantially larger $\nu_e/\bar{\nu}_e$ heating rate and efficiency. This produces a more intense outflow of unbound matter with higher total per baryon energies accounting for its greater energetics in F15.79.

The late energy uptakes exhibited by F15.78 at 1.2 and 1.55 s and by F15.79 at 1.65 s are caused by transient rearrangements in the accretion streams which are stochastic in nature and seem unrelated directly to differences in the progenitor structure. However, they provide well-isolated examples of the connection between accretion streams and the growth of the explosion energy.

The differences in the unbound mass of 56 Ni based on the limited α -reaction network are consistent with the different explosion energies resulting in $1.4 \times 10^{-2}~M_{\odot}$ of 56 Ni for F15.78 and $3.2 \times 10^{-2}~M_{\odot}$ in F15.79 with the more-energetic explosion. The structure of the Si shell in the 15.78 M_{\odot} progenitor leads to a relatively large amount of unburnt 28 Si to become unbound in F15.78 and possibly a larger 44 Ti/ 56 Ni mass ratio than F15.79. In both models the ejecta are mostly moderately proton rich, but small amounts of material with more extreme values of Y_e ranging from 0.46 to 0.61 become unbound at late times, with F15.78 exhibiting higher values of Y_e in the unbound material than F15.79.

We speculate on what differences we might expect had our two simulations been performed in 3D rather than 2D. 2D and 3D simulations performed for the same progenitor indicate that shock revival, in most cases, is a little less robust in 3D (Hanke et al. 2013; Tamborra et al. 2014; Lentz et al. 2015; Melson et al. 2015). An exception is Nagakura et al. (2019) who found that their 19 M_{\odot} progenitor exploded slightly earlier in 3D than in 2D. The shocks, once revived, however, tend to be more energetic in 3D, at least in the few cases where the comparison has extended far enough in time. A detailed analysis of the 2D versus 3D dynamics of shock propagation was provided by Muller (2015). Without repeating his analysis here, he found, on the basis of 2D and 3D simulations initiated from a 11.5 M_{\odot} progenitor, that the mass outflow rate was greater in 3D despite similar heating rates, due to the smaller binding energy of matter at the gain radius. Along with the greater mass outflow, more enthalpy (though not mass-specific enthalpy) was transported to the shock in 3D relative to its 2D counterpart, strengthening the former relative to the latter. These 2D–3D differences, extrapolated to our models, would suggest that shock revival for F15.78, being very robust, would probably be unaffected, while in F15.79 it might be a little more delayed. The shocks, assuming the results of Muller (2015) hold generally, would be more energetic and the remanent masses would likely be smaller.

This research was supported by the U.S. Department of Energy, Offices of Nuclear Physics and Advanced Scientific Computing Research, the NASA Astrophysics Theory Program (grant No. NNH11AQ72I), and the National Science

Foundation PetaApps Program (grant Nos. OCI-0749242, OCI-0749204, and OCI-0749248), Nuclear Theory Program (Nos. PHY-1913531 and PHY-1516197) and Stellar Astronomy and Astrophysics program (No. AST-0653376). This research used resources of the National Energy Research Scientific Computing Center (NERSC), a U.S. Department of Energy Office of Science User Facility located at Lawrence Berkeley National Laboratory, operated under contract No. DE-AC02-05CH11231. This research used resources of the Oak Ridge Leadership Computing Facility at Oak Ridge National Laboratory. Research at Oak Ridge National Laboratory is supported under contract No. DE-AC05-00OR22725 from the Office of Science of the U.S. Department of Energy to UT-Battelle, LLC.

Facilities: NERSC, OLCF.

Software: CHIMERA(Bruenn et al. 2020).

ORCID iDs

Stephen W. Bruenn https://orcid.org/0000-0003-0999-5297

Andre Sieverding https://orcid.org/0000-0001-8235-5910

Eric J. Lentz https://orcid.org/0000-0002-5231-0532

Tuguldur Sukhbold https://orcid.org/0000-0002-1728-1561

W. Raphael Hix https://orcid.org/0000-0002-9481-9126

Leah N. Huk https://orcid.org/0000-0002-1530-7297

J. Austin Harris https://orcid.org/0000-0003-3023-7140

O. E. Bronson Messer https://orcid.org/0000-0002-5358-5415

Anthony Mezzacappa https://orcid.org/0000-0001-9816-9741

References

```
Abdikamalov, E., Zhaksylykov, A., Radice, D., & Berdibek, S. 2016, MNRAS,
Blondin, J., Mezzacappa, A., & DeMarino, C. 2003, ApJ, 584, 971
Boccioli, L., Roberti, L., Limongi, M., Mathews, G. J., & Chieffi, A. 2022,
   arXiv:2207.08361
Bollig, R., Yadav, N., Kresse, D., et al. 2021, ApJ, 915, 28
Bruenn, S. W., Blondin, J. M., Hix, W. R., et al. 2020, ApJS, 248, 11
Bruenn, S. W., Lentz, E. J., Hix, W. R., et al. 2016, ApJ, 818, 123
Bruenn, S. W., Mezzacappa, A., Hix, W. R., et al. 2013, ApJ, 767, L6
Buras, R., Janka, H.-T., Rampp, M., & Kifonidis, K. 2006, A&A, 457, 281
Burrows, A., & Goshy, J. 1993, ApJL, 416, L75
Burrows, A., & Hayes, J. 1996, PhRvL, 76, 352
Burrows, A., Radice, D., & Vartanyan, D. 2019, MNRAS, 485, 3153
Burrows, A., Radice, D., Vartanyan, D., et al. 2020, MNRAS, 491, 2715
Cooperstein, J. 1985, NuPhA, 438, 722
Couch, S. M. 2013, ApJ, 775, 35
Couch, S. M., & Ott, C. D. 2013, ApJL, 778, L7
Couch, S. M., & Ott, C. D. 2015, ApJ, 799, 5
Curtis, S., Ebinger, K., Fröhlich, C., et al. 2019, ApJ, 870, 2
Dolence, J. C., Burrows, A., & Zhang, W. 2015, ApJ, 800, 10
Ebinger, K., Curtis, S., Fröhlich, C., et al. 2019, ApJ, 870, 1
Eichler, M., Nakamura, K., Takiwaki, T., et al. 2018, JPhG, 45, 014001
Ertl, T., Janka, H.-T., Woosley, S. E., Sukhbold, T., & Ugliano, M. 2016, ApJ,
   818, 124
Fernández, R. 2012, ApJ, 749, 142
```

```
Foglizzo, T., Galletti, P., Scheck, L., & Janka, H.-T. 2007, ApJ, 654, 1006
Foglizzo, T., Scheck, L., & Janka, H.-T. 2006, ApJ, 652, 1436
Hamuy, M. 2003, ApJ, 582, 905
Hanke, F., Müller, B., Wongwathanarat, A., Marek, A., & Janka, H.-T. 2013,
   ApJ, 770, 66
Hannestad, S., & Raffelt, G. 1998, ApJ, 507, 339
Harris, J. A., Hix, W. R., Chertkow, M. A., et al. 2017, ApJ, 843, 2
Herant, M., Benz, W., Hix, W. R., Fryer, C. L., & Colgate, S. A. 1994, ApJ,
  435, 339
Hoffman, R. D., Woosley, S. E., Fuller, G. M., & Meyer, B. S. 1996, ApJ,
  460, 478
Janka, H.-T. 1995, APh, 3, 377
Janka, H.-T. 2001, A&A, 368, 527
Janka, H.-T. 2012, ARNPS, 62, 407
Janka, H.-T., Kifonidis, K., & Rampp, M. 2001, in Physics of Neutron Star
   Interiors, ed. D. Blaschke, N. K. Glendenning, & A. Sedrakian, Vol. 578
  (Berlin: Springer), 333
Janka, H.-T., & Müller, E. 1996, A&A, 306, 167
Kraichnan, R. H. 1967, PhFl, 10, 1417
Landfield, R. E. 2018, PhD thesis, Univ. of Tennessee
Lentz, E. J., Bruenn, S. W., Hix, W. R., et al. 2015, ApJL, 807, L31
Martinez, L., Anderson, J. P., Bersten, M. C., et al. 2022, A&A, 660, A42
Melson, T., Janka, H.-T., & Marek, A. 2015, ApJL, 801, L24
Muller, B. 2015, MNRAS, 453, 287
Müller, B. 2016, PASA, 33, e048
Muller, B., Heger, A., Liptai, D., & Cameron, J. B. 2016, MNRAS, 460, 742
Müller, B., & Janka, H.-T. 2014, ApJ, 788, 82
Muller, B., & Janka, H.-T. 2015, MNRAS, 448, 2141
Müller, B., Janka, H.-T., & Marek, A. 2012, ApJ, 756, 84
Muller, B., Melson, T., Heger, A., & Janka, H.-T. 2017, MNRAS, 472, 491
Nagakura, H., Burrows, A., Radice, D., & Vartanyan, D. 2019, MNRAS,
O'Connor, E., & Ott, C. D. 2011, ApJ, 730, 70
O'Connor, E., & Ott, C. D. 2013, ApJ, 762, 126
Ohnishi, N., Kotake, K., & Yamada, S. 2006, ApJ, 641, 1018
Ott, C. D., Roberts, L. F., da Silva Schneider, A., et al. 2018, ApJL, 855, L3
Özel, F., & Freire, P. 2016, ARA&A, 54, 401
Özel, F., Psaltis, D., Narayan, R., & Santos Villarreal, A. 2012, ApJ, 757,
Scheck, L., Janka, H.-T., Foglizzo, T., & Kifonidis, K. 2008, A&A, 477, 931
Schwab, J., Podsiadlowski, P., & Rappaport, S. 2010, ApJ, 719, 722
Sieverding, A., Müller, B., & Qian, Y. Z. 2020, ApJ, 904, 163
Smartt, S. J. 2009, ARA&A, 47, 63
Smartt, S. J. 2015, PASA, 32, 16
Steiner, A. W., Hempel, M., & Fischer, T. 2013, ApJ, 774, 17
Sukhbold, T., Woosley, S. E., & Heger, A. 2018, ApJ, 860, 93
Summa, A., Hanke, F., Janka, H.-T., et al. 2016, ApJ, 825, 6
Suwa, Y., Yamada, S., Takiwaki, T., & Kotake, K. 2016, ApJ, 816, 43
Tamborra, I., Hanke, F., Janka, H.-T., et al. 2014, ApJ, 792, 96
Thompson, T. A., Quataert, E., & Burrows, A. 2005, ApJ, 620, 861
Timmes, F. X., Woosley, S. E., & Weaver, T. A. 1996, ApJ, 457, 834
Ugliano, M., Janka, H.-T., Marek, A., & Arcones, A. 2012, ApJ, 757, 69
Vartanyan, D., Burrows, A., Radice, D., Skinner, M. A., & Dolence, J. 2018,
   MNRAS, 477, 3091
Vartanyan, D., Burrows, A., Radice, D., Skinner, M. A., & Dolence, J. 2019,
   MNRAS, 482, 351
Vartanyan, D., Laplace, E., Renzo, M., et al. 2021, ApJL, 916, L5
Wanajo, S., Müller, B., Janka, H.-T., & Heger, A. 2018, ApJ, 852, 40
Wang, T., Vartanyan, D., Burrows, A., & Coleman, M. S. B. 2022, MNRAS,
  517, 543
Woosley, S. E., & Heger, A. 2007, PhR, 442, 269
Woosley, S. E., Heger, A., & Weaver, T. A. 2002, RvMP, 74, 1015
Xiong, Z., Sieverding, A., Sen, M., & Qian, Y.-Z. 2020, ApJ, 900, 144
Yamasaki, T., & Yamada, S. 2007, ApJ, 656, 1019
```